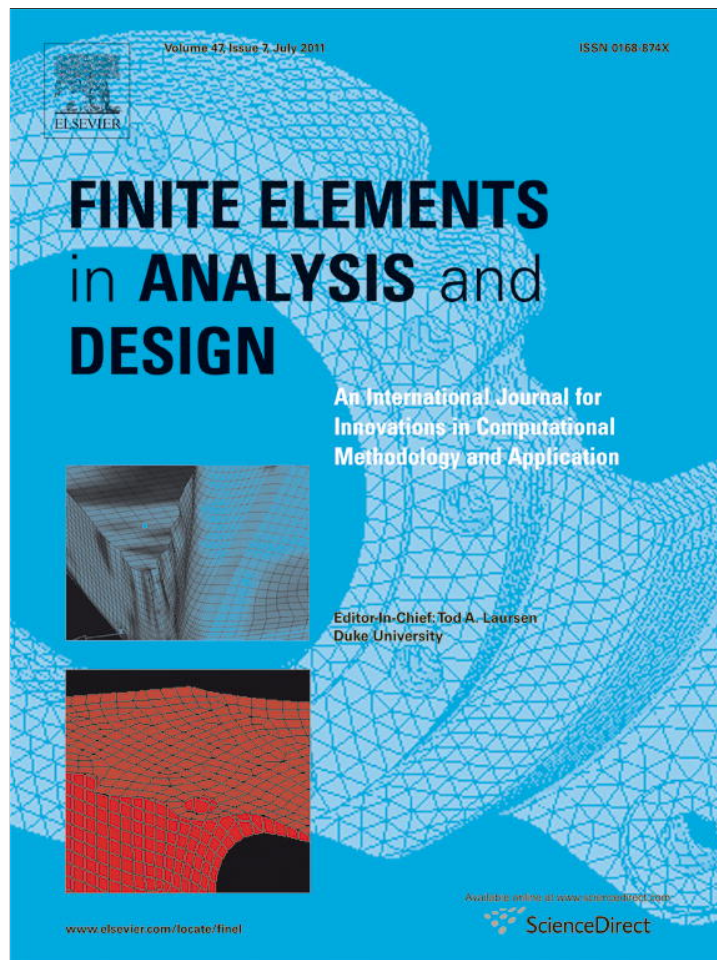


Provided for non-commercial research and education use.
Not for reproduction, distribution or commercial use.



This article appeared in a journal published by Elsevier. The attached copy is furnished to the author for internal non-commercial research and education use, including for instruction at the authors institution and sharing with colleagues.

Other uses, including reproduction and distribution, or selling or licensing copies, or posting to personal, institutional or third party websites are prohibited.

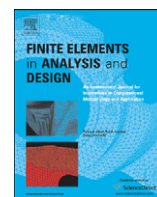
In most cases authors are permitted to post their version of the article (e.g. in Word or Tex form) to their personal website or institutional repository. Authors requiring further information regarding Elsevier's archiving and manuscript policies are encouraged to visit:

<http://www.elsevier.com/copyright>



Contents lists available at ScienceDirect

Finite Elements in Analysis and Design

journal homepage: www.elsevier.com/locate/finel

Analysis of anisotropic Mindlin plate model by continuous and non-continuous GFEM

Paulo de Tarso R. Mendonça*, Clovis S. de Barcellos*, Diego Amadeu F. Torres

Group of Mechanical Analysis and Design - GRANTE, Department of Mechanical Engineering, Federal University of Santa Catarina, 88040-900 Florianópolis, SC, Brazil

ARTICLE INFO

Article history:

Received 22 August 2010

Received in revised form

31 January 2011

Accepted 18 February 2011

Available online 21 March 2011

Keywords:

Generalized finite element method

Partition of unity method

Mindlin plate FEM

 C^k approximation functions

Anisotropic laminated plates

In-plane continuous stresses

ABSTRACT

This paper presents a generalized finite element formulation with arbitrarily continuous unknown fields for static bending analysis of anisotropic laminated plates based on Mindlin's kinematical model. This consist of an extension of the work of Barcellos et al. (2009) [39] to moderate thick plates and also exploits the properties of smooth approximation functions built from the Duarte extension of Edwards' procedure (Duarte et al., 2006 [44]) in the framework of the so-called C^k -GFEM. The strategy is suitable for p - and k -enrichments on a fixed mesh of finite elements and its accuracy is evaluated in numerical experiments against analytical solutions. The performance is compared to the standard C^0 -GFEM/XFEM approach and several topics of concern are investigated, such as the required number of integration points for the computation of the element matrices, the influence of the degree of polynomial enrichment, the degree of inter-element continuity chosen for the basis functions, the effect of laminate thickness and the sensitivity to mesh distortions and its relation with the stiffness matrix conditioning. Errors in-plane and transverse shear stresses are computed. The smoothness contributes to the accuracy in terms of the energy norm and furnishes better derivatives of the solution fields, leading to better post-processed transverse shear stresses, which can be further improved by a proposed heuristic procedure.

© 2011 Elsevier B.V. All rights reserved.

1. Introduction

Since the beginning of its development, the finite element method (FEM) has been based, mostly, on C^0 continuous approximations for the primary variables, even when modeling variational problems involving smoother variables. In approaching typical problems such as elasticity in continuous fields, which has C^0 variational formulation, the C^0 FEM is routinely applied. However, certain models, like the bending models for plates/shells of Kirchhoff, and more recently the higher-order model for plate bending of Reddy, among others, have one or more kinematic variables in the C^1 space. Therefore, since the early years of the FEM, numerous researchers have proposed several element formulations based mostly on the Kirchhoff hypothesis for thin plates/shells and Mindlin/Reissner hypothesis for the moderately thick ones. If the plate is moderately thick, it must be modeled by a higher-order theory, such as that of Mindlin. Here, the displacement field is described by the transversal displacement, w , and the rotations, ψ_x and ψ_y , of the normal to the plate middle plane. In this case, only C^0 is required continuity for the displacement

field and for this reason this model has been dominant in recent decades, e.g. [1], in the finite element community. However, the Mindlin/Reissner plate elements usually exhibit shear locking when the plate thickness decreases as the Kirchhoff constraints cease to be fulfilled over the entire element. To avoid the locking, the early elements used reduced or selective reduced integration which may lead to zero-energy modes that can be eliminated by hourglass control [2]. Other attempts were based on mixed and hybrid formulations, see e.g. [3,4], which must satisfy the Ladysensenskaja–Babuška–Brezzi (LBB) condition in order to be stable. Since they are complex and computationally expensive, these are not very popular in commercial codes. Other approaches to improve the transverse shear locking include the assumed natural strain (ANS) proposed by [5], the discrete-shear-gap (DSG) of [6], and stabilized conforming nodal integration (SCNI) [7,8]. In addition, special formulations for the Kirchhoff model have been developed, for example the discrete Kirchhoff triangular (DKT) element [2], based on the imposition of zero transverse shear deformation at specific points of the element.

On the other hand, there have been several contributions for removing shear locking through meshfree methods like, e.g. [9–14]. The meshless methods concepts began with the smoothed particle hydrodynamics method (SPH) [15], which was followed by the diffuse element method (DEM) [16], wavelet Galerkin method [17], element free Galerkin method (EFGM) [18], reproducing kernel

* Corresponding authors. Tel.: +55 48 3721 9899.

E-mail addresses: mendonca@grante.ufsc.br (P.T.R. Mendonça), clovis@grante.ufsc.br (C.S. de Barcellos), diego.amadeu@gmail.com (D.A.F. Torres).

particle method (RKPM) [19], meshless local Petrov–Galerkin method (MLPG) [20], natural element method [21], partition of unity method (PUM) [22], and hp -clouds methods, e.g. [23,24], among others. The latter allows a natural and effective inclusion of p -adaptivity, avoiding the construction of functions by sophisticated hierarchical techniques, and for this reason they were used in [25,9]. The advantages of meshless procedures need to be balanced against increased computational cost, since a background mesh, usually triangular, is still needed for integration purposes. Then, at each integration point, the partition of unity must be computed and, since the cardinality at each point is arbitrary, one needs to search for every cloud which covers such a point. In addition, all these meshless methods present some disadvantages regarding the imposition of boundary conditions and high computational costs.

In order to reduce the numerical integration and implementation difficulties of meshfree methods, Oden et al. [26] proposed that, instead of using circles to define the clouds¹ around each node as performed in the hp -clouds method [24], it would be more convenient to use a mesh of linear finite element in such a way that the cloud associated with a node “ i ” would be built by the union of the finite elements connected to this node. This concept greatly reduces the number of floating point operations, since the partition of unity is known beforehand and allows the use of standard integration routines to integrate the element matrices. This new scheme led to an instance of the generalized finite element methods (GFEM). Independently, Melenk, Babuška and coworkers proposed essentially the same procedure, initially named the special finite element method, then the GFEM [27], and later, the partition of unity finite element method [28]. Belytschko and Black [29] and Moës et al. [30] applied the same strategy, as reported in [31], to represent discontinuous solutions and this was called the extended finite element method (XFEM). The p -enrichment in GFEM/XFEM, as in other meshfree methods like hp -clouds, is performed nodally, which suggests an adaptive scheme to provide automatic control of approximation errors. Several important contributions have been proposed, as follows. Strouboulis et al. [32,33] exploit the capabilities provided by GFEM enrichment using mesh-based handbook functions generated from canonical domains, containing microstructural features, for materials with internal cracks and voids. Duarte and Babuška [34] used p -orthotropic enrichment aligned to the optimal direction of enrichment in the sense of the direction that gives the largest reductions in the discretization error for a given number of additional degrees of freedom. Barros et al. [35] proposed an error estimator and implemented p -adaptivity for C^0 -GFEM and Barros et al. [36] extended the p -adaptivity for C^k -GFEM using arbitrary polygonal clouds. Simone et al. [37] exploited the partition of unity property to explicitly model grain boundaries in polycrystal materials. Garcia et al. [38] proposed the using of pseudo-tangent planes to separate the geometric description from the approximation space, in such a fashion that the enrichment is defined in a locally undistorted domain, for thick shells. Barcellos et al. [39] investigated some features of the C^k -GFEM applied to Kirchhoff plate model and Torres et al. [40] verified the convergence behavior of a C^0 -GFEM formulation derived for adaptive piezoelectric laminated plates.

In these procedures, the solution improvement is reached by performing extrinsic nodal enrichment without excessively increasing the computational effort even in the presence of stress concentration, e.g. [41], thus reducing the possible need to

perform a mesh refinement in addressing this type of problem if the initial mesh is suitably designed.

It should be noted that the extrinsic enrichment requires additional global degrees of freedom but the discontinuity does not exist when different extrinsic enrichment functions are used at different discrete points, differently of the intrinsic enrichment of Liu et al. [19], for instance, which introduces reproducibility of basis functions without additional global degrees of freedom but needing to enlarge non-locality of the functions since discontinuity exists when enrichment functions vary in space even if C^∞ functions are used.

In performing analysis using conventional Mindlin plate finite elements, one faces discontinuous stresses between elements which may be related to the quality of the mesh, and these have to be dealt with by post-processing using, frequently, heuristic procedures. In order to be able to have continuous stress distributions one needs C^1 approximation functions. Toward this end, Edwards [42,43] proposed a scheme in which a finite element mesh is used to build arbitrarily smooth approximation functions which have the same support as the corresponding global finite element Lagrangian shape functions on the same mesh. But this scheme has an important restriction as it requires the clouds to be convex, which is not always possible to guarantee. In order to remove this limitation, Duarte et al. [44] proposed the use of the so-called Boolean R-function of Shapiro [46,45]. Barros et al. [36] later discussed this procedure to address linear elasticity problems and Barcellos et al. [39] applied it to the Kirchhoff plate model. The arbitrary continuity depends on the type of selected edge functions and on the value of a parameter of the Boolean function.

In this paper, the extension of Edwards' procedure proposed by Duarte is explored for convex and non-convex supports (clouds), with the aid of the R-functions [45,46], on GFEM to generate C^k approximation functions in triangular unstructured meshes. This set of approximation functions is applied to solve a Mindlin plate problem, and the influence of the type of integration rules, as well as the mesh distortions, is analyzed. In addition, different types of cloud edge functions are implemented and tested. The Mindlin model is used in most commercial codes, in spite of the fact that it is not the most appropriate for laminated composite plates [47]. The characteristics of the GFEM inhibit its comparison with the standard FEM, particularly with the formulations available in commercial programs. These formulations are characterized by low-order polynomial basis, in contrast with the high orders usually associated with GFEM. In regular problems, the rate of convergence in p -enrichment, which is naturally performed in GFEM, is twice the rate of the h -refinement [48] usually present in commercial codes. Additionally, even for the same polynomial order, the GFEM also uses enrichments defined in global coordinates, in contrast to conventional p -FEM. Therefore, the most suitable formulation to evaluate the performance of the continuous formulation is the standard GFEM. Throughout this paper, the standard GFEM/XFEM, based on C^0 partition of unity, and the continuous GFEM, will be referred to as C^0 -GFEM and C^k -GFEM, respectively. It is verified in this example problem that both continuities may accept high distortions with acceptable errors if properly enriched. Also, since numerical integration on meshless methods are still of concern [49], some investigation regarding the required orders of integration is carried out.

The remainder of this paper is outlined as follows. Section 2 summarizes the partition of unity concepts and their enrichment. It also explains the construction of weight functions with the use of appropriate R-functions in order to achieve approximation functions with C^∞ and C^k continuity for arbitrary domain triangulation. Section 3 gives a summary of the Mindlin plate model for anisotropic laminates. Here, one of the reasons for

¹ A cloud is loosely defined as an open compact support around each node, with the property that the countable collection of clouds defines a covering of the domain.

moving to this new goal was to investigate the integrability of the Mindlin stiffness matrix with these new approximation functions. Before moving on to better laminated bending models requiring higher continuity, it is important to investigate their performance in the Mindlin model since the first derivatives of the functions present fewer oscillations of smaller magnitude, differently to the behavior verified for the second derivatives, as was shown in [39]. Section 4 reports the results of the proposed formulation in order to test its behavior under several conditions. Firstly, it is of concern to assess the performance of the approximation functions by performing verification, comparing the discretization procedure with exact analytical solutions to the same mathematical model. The computation of accurate transverse shear stresses in laminates is also investigated and, even considering an old and well-established model like the Mindlin model, the degree of the basis functions utilized and their inter-element smoothness (or lack of it) have a strong influence on the quality of the transverse shear stresses that can be computed or extracted. Moreover, an improvement to the procedure of stress post-processing is proposed and verified. The computational efficiency of the C^k -GFEM is compared to the standard C^0 -GFEM in such a way that the basis functions generated by smooth and C^0 -GFEM are identified and compared for each type of enrichment. The influence over the condition number of the stiffness matrix is shown. Finally, in Section 5 some conclusions are outlined.

2. Partition of unity and approximation functions

The C^k -GFEM with arbitrary continuity can be considered a special instance of the hp -cloud in which each cloud has an arbitrary polygonal boundary and the weight functions are built in such a way as to guarantee the required continuity. Let us consider the plate mid-surface as an open bounded domain, $\Omega \subset \mathcal{R}^2(\mathbf{x})$, which is partitioned in a linear triangular mesh, $\{\mathcal{K}_e\}_{e=1}^{NE}$ (NE being the number of elements \mathcal{K}_e), using N nodes with coordinates $\{\mathbf{x}_\alpha\}_{\alpha=1}^N$. For each of these nodes one considers as *cloud*, $\omega_\alpha, \alpha = 1, \dots, N$, the union of the triangular elements which share it so that N clouds is an open covering, \mathfrak{I}_N , of the domain Ω .

Consider a set of functions, $\mathcal{W}_\alpha(\mathbf{x}) \subset C_0^k(\omega_\alpha)$ where $\alpha = 1, \dots, N$, such that each one of them has the associated cloud ω_α as its compact support and is denoted as a *weight function*. Next, one uses Shepard's moving least squares method [50] to obtain the set of functions $\{\varphi_\alpha(\mathbf{x})\}_{\alpha=1}^N$ as

$$\varphi_\alpha(\mathbf{x}) = \frac{\mathcal{W}_\alpha(\mathbf{x})}{\sum_{\beta(\mathbf{x})} \mathcal{W}_\beta(\mathbf{x})}, \quad \beta(\mathbf{x}) \in \{\gamma \mid \mathcal{W}_\gamma(\mathbf{x}) \neq 0\} \quad (1)$$

One can easily verify that this set, $\{\varphi_\alpha(\mathbf{x})\}, \alpha = 1, \dots, N$, is such that $\varphi_\alpha(\mathbf{x}) \in C_0^k(\omega_\alpha), k \geq 0$ and $\sum_{\alpha=1}^N \varphi_\alpha(\mathbf{x}) = 1, \forall \mathbf{x} \in \Omega$, and every compact subset of Ω intersects only a finite number of supports. Therefore, it is a partition of unity (PoU) subordinate to the covering \mathfrak{I}_N , where the first requirement is met because each $\varphi_\alpha(\mathbf{x})$ is, at least, k times continuously differentiable and is non-zero only over its respective cloud ω_α . Moreover, it shares the same features as the standard finite element method regarding the domain partition and integration procedures. It is clear that the continuity of the PoU is the same as the weight function. Therefore, the weight function \mathcal{W}_α must satisfy some conditions which will impart a great influence on the approximation process. Firstly, they must have the required continuity k , and, secondly, the resulting PoU should have reasonable integrability properties, and be able to, at least, represent a constant solution. The importance of adequate continuity has been previously reported in [51].

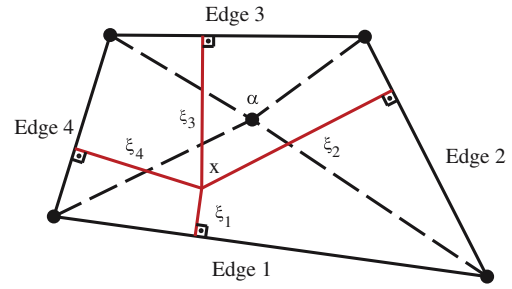


Fig. 1. Illustration of a cloud ω_α built by four triangular elements.

The weight functions are, in the case of convex clouds, constructed by the product of the so-called *cloud edge functions*, $\varepsilon_{\alpha,j}[\xi_j(\mathbf{x})]$, where $\xi_j(\mathbf{x})$ is a parametric normal coordinate from the edge, as is the case of the internal node α in Fig. 1. Here, for the associated cloud, ω_α , the boundary is the closed polygonal built with the edges of the cloud elements that are not connected to the node \mathbf{x}_α . A similar definition is used for the clouds at the boundary of the domain. The *cloud edge functions* play therefore an essential role as part of the PoU building process, that is, they must have at least the desired C^k continuity, $k \geq 0$, with k being an arbitrary integer. In order for the weight function to be unitary² at node \mathbf{x}_α , all of the M_α edge functions of the cloud are required to have the unitary value at this node. Hence, the weight function can be expressed as

$$\mathcal{W}_\alpha(\mathbf{x}) := \prod_{j=1}^{M_\alpha} \varepsilon_{\alpha,j}(\xi_j) \quad (2)$$

Herein, two kinds of *cloud edge functions*, $\varepsilon_{\alpha,j}$, are used. The first type are the polynomials of degree $P, P \geq k + 1$, such that the function together with its first k normal derivatives approach zero as a point reaches its edge, j , as explained in [39]. It is given by

$$\varepsilon_{\alpha,j}[\xi_j(\mathbf{x})] = \begin{cases} (\xi_j/h_{\alpha,j})^P & \text{if } \xi_j > 0 \\ 0 & \text{otherwise} \end{cases} \quad (3)$$

where $h_{\alpha,j}$ is the normal distance of the cloud node α to the edge and $\xi_j(\mathbf{x})$ is the distance of a point \mathbf{x} to the cloud edge j , as shown in Fig. 1.

The second type of edge function is an exponential with an adequate decay, as proposed by Edwards [42]

$$\varepsilon_{\alpha,j}[\xi_j(\mathbf{x})] = \begin{cases} Ae^{-(\xi_j/B)^\gamma} & \text{if } \xi_j > 0 \\ 0 & \text{otherwise} \end{cases} \quad (4)$$

with constants A and B given by

$$A = e^{((1-2^\gamma)/\log_e \beta)^{-1}} \quad \text{and} \quad B = h_{\alpha,j} \left(\frac{\log_e \beta}{1-2^\gamma} \right)^{1/\gamma}$$

β and γ are constants to be specified and, herein, values of $\gamma = 0.6$ and $\beta = 0.3$ are used following Duarte et al. [44]. The parameter β defines how fast the edge function decays to zero toward the edge j and it is given by

$$\beta = \frac{\varepsilon_{\alpha,j} \left(\frac{h_{\alpha,j}}{2} \right)}{\varepsilon_{\alpha,j}(h_{\alpha,j})} \quad (5)$$

For convex clouds, this exponential edge function leads to C^∞ weighting functions, and therefore to C^∞ PoU. In the case of non-convex clouds as illustrated in Fig. 2, each pair of non-convex edges has the product of their edge functions substituted by an

² The weight functions are required to be unitary at their node as a normalization of their values, which is important in avoiding numerical round-off errors in extremely distorted meshes.

R-function “or” with two arguments, f_1 and f_2 , denoted by $(f_1 \vee_0^k f_2)$, defined as

$$(f_1 \vee_0^k f_2) := \left(f_1 + f_2 + \sqrt{f_1^2 + f_2^2} \right) (f_1^2 + f_2^2)^{k/2} \quad (6)$$

where k is a positive integer, as proposed by Duarte et al. [44]. This function is real-valued and its sign is completely determined by the signs of its arguments. It is also analytic everywhere except at the origin, where it is k times differentiable, i.e., it belongs to $C^k(\Omega)$ [46]. Particularly, if $f_1 \geq 0$ and $f_2 \geq 0$ define two regions in \mathcal{R}^2 , then

- $(f_1 \vee_0^k f_2) \geq 0$ and,
- $(f_1 \vee_0^k f_2) > 0$ if $f_1 > 0$ or $f_2 > 0$.

where the arguments, f_i , can also describe curved edges.

Specifically, if a cloud ω_α has sides m and n identified as non-convex, their edge functions $\varepsilon_{\alpha,m}$ and $\varepsilon_{\alpha,n}$ are substituted by

$$\varepsilon_{\alpha,mn}^{nc}(\mathbf{x}) := \frac{\varepsilon_{\alpha,m}(\mathbf{x}) \vee_0^k \varepsilon_{\alpha,n}(\mathbf{x})}{\varepsilon_{\alpha,m}(\mathbf{x}_\alpha) \vee_0^k \varepsilon_{\alpha,n}(\mathbf{x}_\alpha)} \quad (7)$$

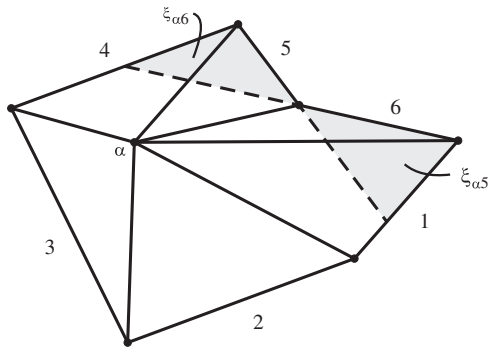


Fig. 2. Non-convex cloud where the Edwards functions are null in the hatched areas.

where the parameter k is chosen according to the desired degree of smoothness. The resultant cloud edge function is also scaled by its value at the cloud node \mathbf{x}_α , such that the resulting function is unitary at node α . This modified cloud edge function is used to build a C^k weight function in a similar fashion as in (2), but where $\varepsilon_{\alpha,mn}^{nc}(\mathbf{x})$ replaces both $\varepsilon_{\alpha,m}(\mathbf{x})$ and $\varepsilon_{\alpha,n}(\mathbf{x})$.

Consider the L-shaped cloud shown in Fig. 3(a), defined in terms of the dimension a . Its node is located at $(x,y) = (0.8a; 0.8a)$. The cloud possesses a pair of non-convex edges, 1 and 2. Fig. 3(b) shows the polynomial edge function $\varepsilon_{\alpha,1}(\mathbf{x}) = (y/h_1)^P$, where $h_1 = 0.8a$ and $P=2$, associated with edge 1. Figs. 3(c) and (d) show the edge functions for the pair of non-convex edges 1 and 2, given by (7) with $k=0$ and 2, respectively.

In sequence, Shepard's formula (1) is employed to build a partition of unity using the C^k weighting functions, $\mathcal{W}_\alpha(\mathbf{x})$. This PoU is therefore at least k -times continuously differentiable everywhere in the domain Ω .

Finally, the partition of unity is employed to span the approximation subspace along the same scheme as that of the hp -clouds method, that is, for each cloud $\omega_\alpha, \alpha = 1, \dots, N$, one chooses a set of enrichment functions, $\{L_{i\alpha}\}_{i \in \mathcal{I}(\alpha)}$, where $\mathcal{I}(\alpha), \alpha = 1, \dots, N$, is an index set. The enrichment functions may be chosen as generalized harmonic functions, anisotropic functions, singular solutions of the specific problem to be analyzed as well as polynomials. The local function subspaces are denoted by $\chi_\alpha(\omega_\alpha) = \text{span}\{L_{i\alpha}\}_{i \in \mathcal{I}(\alpha)}$ and may also be enriched only locally according to an adaptive procedure.

Here, without loss of generality, one performs only polynomial enrichments because of the nature of the domain geometry and the type of the loading. Thus, one has

$$\mathcal{P}_p(\omega_\alpha) \subset \chi_\alpha^p(\omega_\alpha) \quad (8)$$

where \mathcal{P}_p denotes the space of polynomials a degree less than or equal to p . For scaling purposes, a cloud characteristic length h_α is defined as the largest distance from the node \mathbf{x}_α to each of the cloud ω_α edges. Thus, one defines the normalized coordinate $\bar{\mathbf{x}}$ as

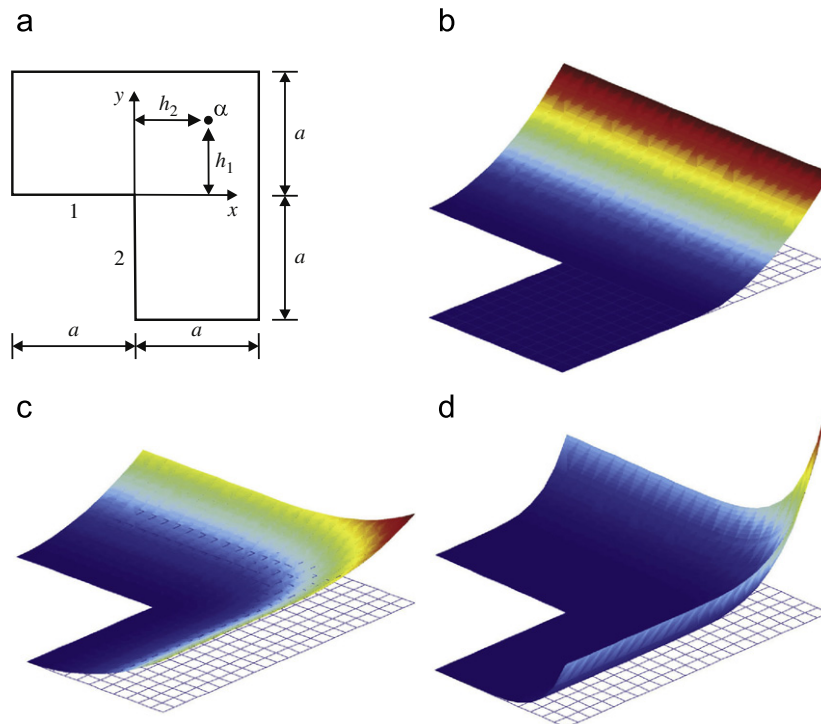


Fig. 3. Visualization of edge functions. (a) L-shaped domain; (b) polynomial edge function; (c) edge function for the non-convex edges, $k=0$; (d) edge function for the non-convex edges, $k=2$.

$\bar{\mathbf{x}} = (\mathbf{x} - \mathbf{x}_\alpha) / h_\alpha$. This normalization renders the enrichment functions non-dimensional.

The enrichment sets considered in this work are the following:

Linear enrichment : $L_{ix} = [1, \bar{x}, \bar{y}]$
 Quadratic enrichment : $L_{ix} = [1, \bar{x}, \bar{y}, \bar{x}^2, \bar{x}\bar{y}, \bar{y}^2]$
 Cubic enrichment : $L_{ix} = [1, \bar{x}, \bar{y}, \bar{x}^2, \bar{x}\bar{y}, \bar{y}^2, \bar{x}^3, \bar{x}^2\bar{y}, \bar{x}\bar{y}^2, \bar{y}^3]$
 Quartic enrichment : $L_{ix} = [1, \bar{x}, \bar{y}, \bar{x}^2, \bar{x}\bar{y}, \bar{y}^2, \bar{x}^3, \bar{x}^2\bar{y}, \bar{x}\bar{y}^2, \bar{y}^3, \bar{x}^4, \bar{x}^3\bar{y}, \bar{x}^2\bar{y}^2, \bar{x}\bar{y}^3, \bar{y}^4]$ (9)

The C^k -GFEM PoU functions cannot represent linear or higher-order monomials, as does the linear tent functions used in C^0 -GFEM. That is, there is, for instance, no set of coefficients a_α^x such that $\sum_{\alpha=1}^N a_\alpha^x \varphi_\alpha = x$. Therefore, the representation of linear monomials is only possible with the use of enriched functions. For example, with the use of the set $(x\varphi_\alpha)$ one has

$$\sum_{\alpha=1}^N a_\alpha^x (x\varphi_\alpha) = x \sum_{\alpha=1}^N a_\alpha^x \varphi_\alpha$$

If all the coefficients a_α^x are taken to be unity, the right hand side becomes equal to x . In general, the C^k -GFEM PoU enriched with an arbitrary polynomial $x^r y^s$ is only able to represent polynomials of the same degree

$$\sum_{\alpha=1}^N a_\alpha^x (x^r y^s \varphi_\alpha) = x^r y^s \quad (10)$$

The set of approximation functions in a cloud is $\{\varphi_\alpha\} = \varphi_\alpha \times \{L_{ix}\}$, and it defines the approximation space $\bar{\chi}(\omega_\alpha) = \text{span}\{\varphi_\alpha \times \{L_{ix}\}\}$. It can be seen from (10) that

$$\bar{\chi}(\omega_\alpha) = \text{span}\{L_{ix}\} \quad (11)$$

If p ($p = r + s$) is the largest polynomial degree in the set $\{L_{ix}\}$, the dimensions of the basis in $\bar{\chi}$ are 3, 6, 10 and 15, respectively, for $p = 1, 2, 3$ and 4 for C^k -GFEM. This is different for C^0 -GFEM. In this latter case, its PoU is defined by linear functions and, also, coefficients a_α^x and a_α^y exist such that

$$\sum_{\alpha=1}^N a_\alpha^x \varphi_\alpha = x$$

$$\sum_{\alpha=1}^N a_\alpha^y \varphi_\alpha = y \quad (12)$$

Therefore, the C^0 -GFEM PoU enriched by $x^r y^s$ are such that it is possible to have

$$\sum_{\alpha=1}^N a_\alpha^x (x^r y^s \varphi_\alpha) = x^{r+1} y^s$$

$$\sum_{\alpha=1}^N a_\alpha^y (x^r y^s \varphi_\alpha) = x^r y^{s+1} \quad (13)$$

In this case an enrichment set of degree p generates a basis of degree $b = p + 1$. Thus, for a given degree of enrichment, the C^0 -GFEM generates a richer approximation space than the C^k -GFEM. However, the set of basis functions in the C^0 -GFEM is linearly dependent, as a consequence of the fact that its PoU and enrichment functions are both polynomials [52]. This results in a stiffness matrix with rank deficiency. On the other hand, in C^k -GFEM, the PoU is a rational function which cannot be represented by a finite linear combination of monomials. Hence, the set $\{\varphi_\alpha \times \{L_{ix}\}\}$ is linearly independent and the stiffness matrix has the proper rank.

In the presence of an arbitrarily shaped domain, this kind of enrichment only can be performed for the interior clouds. The boundary clouds should be enriched in a modified scheme, taking into account the prescribed boundary conditions. One such choice was presented by Garcia et al. [23], where similar enrichments are

applied in a local coordinate system in which one of the axes is normal to the boundary. Another choice is to modify the boundary weight function in order to satisfy the boundary conditions explicitly as will be detailed in a forthcoming paper.

3. Mindlin plate model

3.1. Equilibrium equations

In this section, the Mindlin plate model is briefly reviewed. This is a plate bending model first proposed by Mindlin in 1951 [53]. Initially, it was presented as an evolution of the Kirchhoff model, for linear homogeneous isotropic materials in static and dynamic problems, and later expanded to plates and shells of laminates composed of anisotropic layers, widely used in commercial finite element codes, in spite of its mathematical limitations to model these types of structures.

The domain of the problem consists of a region V belonging to a three-dimensional Cartesian coordinate system \mathcal{R}^3 , defined by a constant thickness $t > 0$ and its plane middle surface Ω , limited by a closed contour Γ . Hence, the domain can be described by

$$V = \left\{ \mathbf{q} \in \mathcal{R}^3 \mid z \in \left[-\frac{t}{2}, \frac{t}{2} \right], (x, y) \in \Omega, \Omega \subset \mathcal{R}^2 \right\} \quad (14)$$

for $\mathbf{q} = (x, y, z)$.

The Mindlin model is characterized by a few kinematic hypothesis, which are completely represented in the following first-order expansion, in transverse coordinate z , of the displacement field

$$u(x, y, z) = u^0(x, y) + \psi_x z,$$

$$v(x, y, z) = v^0(x, y) + \psi_y z,$$

$$w(x, y, z) = w(x, y), \quad (15)$$

where u , v , and w are the displacement components along the x , y , and z directions, respectively, $u^0(x, y)$ and $v^0(x, y)$ are in-plane displacements on the middle surface, w is the transverse displacement, and $\psi_x(x, y)$ and $\psi_y(x, y)$ are the rotations undergone by a straight line segment initially normal to the reference surface, about axes x and y , respectively. All these unknowns are called generalized displacements. This expansion represents the assumption that the normal segment remains straight and inextensible. Applying this displacement field to the linear strain–displacement relations implies that the non-vanishing deformation components are the in-plane deformations $\boldsymbol{\varepsilon}(x, y, z) = \{\varepsilon_x, \varepsilon_y, \gamma_{xy}\}^T$ (the superscript T indicates transpose) and transverse shear deformations $\gamma_s(x, y, z) = \{\gamma_{yz}, \gamma_{xz}\}^T$. According to (15), the in-plane and transverse shear deformations are related to the generalized displacements by

$$\boldsymbol{\varepsilon}(x, y, z) = \boldsymbol{\varepsilon}^0(x, y) + z \boldsymbol{\kappa}(x, y),$$

$$\gamma_{yz}(x, y) = \psi_y + \frac{\partial w}{\partial y},$$

$$\gamma_{xz}(x, y) = \psi_x + \frac{\partial w}{\partial x} \quad (16)$$

where $\boldsymbol{\varepsilon}^0$ and $\boldsymbol{\kappa}$ are the membrane deformations and change of curvatures of the middle surface, given by $\boldsymbol{\varepsilon}^0 = \mathbf{L}^0 \mathbf{d}$ and $\boldsymbol{\kappa} = \mathbf{L}^b \mathbf{d}$, and the transverse shear deformations are given by $\gamma_s = \mathbf{L}^s \mathbf{d}$. The generalized displacement vector function \mathbf{d} , and the differential

operators \mathbf{L}^s , \mathbf{L}^o and \mathbf{L}^b are given by

$$\mathbf{L}^o = \begin{bmatrix} \frac{\partial}{\partial x} & 0 & 0 & 0 & 0 \\ 0 & \frac{\partial}{\partial y} & 0 & 0 & 0 \\ \frac{\partial}{\partial y} & \frac{\partial}{\partial x} & 0 & 0 & 0 \end{bmatrix},$$

$$\mathbf{L}^b = \begin{bmatrix} 0 & 0 & 0 & \frac{\partial}{\partial x} & 0 \\ 0 & 0 & 0 & 0 & \frac{\partial}{\partial y} \\ 0 & 0 & 0 & \frac{\partial}{\partial y} & \frac{\partial}{\partial x} \end{bmatrix},$$

$$\mathbf{L}^s = \begin{bmatrix} 0 & 0 & \frac{\partial}{\partial y} & 0 & 1 \\ 0 & 0 & \frac{\partial}{\partial x} & 1 & 0 \end{bmatrix},$$

$$\mathbf{d} = \{u^o, v^o, w, \psi_x, \psi_y\}^T \quad (17)$$

Next, one considers the plate built by a stack of N_l orthotropic layers. The in-plane and transverse shear stress components are denoted by $\boldsymbol{\sigma} = \{\sigma_x, \sigma_y, \sigma_{xy}\}^T$ and $\boldsymbol{\tau}_s = \{\sigma_{yz}, \sigma_{xz}\}^T$, respectively. The generalized Hooke's Law for an arbitrary layer k , in the plane stress state, is expressed by $\boldsymbol{\sigma} = \bar{\mathbf{Q}}\boldsymbol{\varepsilon}$, where $\bar{\mathbf{Q}}$ is the 3×3 reduced stiffness matrix representing the orthotropic layer with its principal material directions arbitrarily oriented with respect to axis x [54]. Similarly, the transverse shear stress-strain relation for an arbitrary layer k is $\boldsymbol{\tau}_s = \mathbf{C}_s\boldsymbol{\gamma}_s$. The resultant in-plane forces $\mathbf{N} = \{N_x, N_y, N_{xy}\}^T$, resulting moments $\mathbf{M} = \{M_x, M_y, M_{xy}\}^T$ and resultant transverse forces $\mathbf{Q} = \{Q_y, Q_x\}^T$ are defined as

$$\mathbf{N} = \int_{z=-t/2}^{t/2} \boldsymbol{\sigma} dz, \quad \mathbf{M} = \int_{z=-t/2}^{t/2} z\boldsymbol{\sigma} dz,$$

$$\mathbf{Q} = \int_{z=-t/2}^{t/2} \boldsymbol{\tau}_s dz \quad (18)$$

Applying the reduced Hooke's Law, these definitions lead to the relation between resultant forces and moments with mid-surface deformations for the laminate

$$\begin{Bmatrix} \mathbf{N} \\ \mathbf{M} \end{Bmatrix} = \begin{bmatrix} \mathbf{A} & \mathbf{B} \\ \mathbf{B} & \mathbf{D} \end{bmatrix} \begin{Bmatrix} \boldsymbol{\varepsilon}^o \\ \boldsymbol{\kappa} \end{Bmatrix} \quad (19)$$

where \mathbf{A}, \mathbf{D} and \mathbf{B} are 3×3 stiffness sub-matrices, all symmetric, representing in-plane, bending and stretch-bending coupling behavior, respectively, of the laminated plate. The transverse forces are given by $\mathbf{Q} = \mathbf{E}\boldsymbol{\gamma}_s$, where the laminate shear stiffness matrix \mathbf{E} is defined with a correction given by a shear factor k_s , such that

$$\mathbf{E} = k_s \sum_{k=1}^{N_l} h_k \mathbf{C}_s^k \quad (20)$$

and h_k and N_l are the k -th layer thickness and the number of layers in the laminate, respectively.

In cases where the laminate is symmetric with respect to its middle surface, the coupling stiffness matrix $\mathbf{B} = \mathbf{0}$ and the bending response is decoupled from the in-plane behavior. The differential equilibrium equations are

$$R_x \equiv \frac{\partial N_x}{\partial x} + \frac{\partial N_{xy}}{\partial y} + \sigma_{xz}|_{-t/2}^{t/2} = 0$$

$$R_y \equiv \frac{\partial N_{xy}}{\partial x} + \frac{\partial N_y}{\partial y} + \sigma_{yz}|_{-t/2}^{t/2} = 0$$

$$R_z \equiv \frac{\partial Q_x}{\partial x} + \frac{\partial Q_y}{\partial y} + q(x,y) = 0$$

$$R_{mx} \equiv \frac{\partial M_x}{\partial x} + \frac{\partial M_{xy}}{\partial y} - Q_x + z\sigma_{xz}|_{-t/2}^{t/2} = 0$$

$$R_{my} \equiv \frac{\partial M_{xy}}{\partial x} + \frac{\partial M_y}{\partial y} - Q_y + z\sigma_{yz}|_{-t/2}^{t/2} = 0 \quad (21)$$

where $q(x,y)$ is the distributed applied normal load. $\sigma_{xz}|_{-t/2}^{t/2}$ stands for $\sigma_{xz}(z=t/2) - \sigma_{xz}(z=-t/2)$. Similarly, one has $\sigma_{yz}|_{-t/2}^{t/2}$. In the cases considered in this paper both faces of the laminate are free from shear loading, such that $\sigma_{xz}|_{-t/2}^{t/2} = \sigma_{yz}|_{-t/2}^{t/2} = 0$. The shear forces Q_x and Q_y can be eliminated from the third equation by using the last two. In the most general cases of non-symmetric laminates, these equations are coupled. For symmetric laminates the system becomes uncoupled, with the bending being described by only the last three equations.

The formulation implemented in this paper is aimed at the general case of laminated plates composed of anisotropic layers, represented by (18)–(21), through a generalized finite element procedure. Therefore, let us start from the bilinear and linear operators

$$G(\mathbf{d}, \delta\mathbf{d}) = \int_{\Omega} \begin{Bmatrix} \delta\boldsymbol{\varepsilon}^o \\ \delta\boldsymbol{\kappa} \end{Bmatrix}^T \begin{bmatrix} \mathbf{A} & \mathbf{B} \\ \mathbf{B} & \mathbf{D} \end{bmatrix} \begin{Bmatrix} \boldsymbol{\varepsilon}^o \\ \boldsymbol{\kappa} \end{Bmatrix} d\Omega + \int_{\Omega} \delta\boldsymbol{\gamma}_c^T \mathbf{E}\boldsymbol{\gamma}_c d\Omega$$

$$l(\delta w) = \int_{\Omega} \delta w q d\Omega \quad (22)$$

Hence, the plate problem can be stated in a weak form as: find $\mathbf{d}(x,y) \in \mathcal{U}_1^5(\Omega)$, such that $G(\mathbf{d}, \delta\mathbf{d}) = l(\delta w)$, for $\forall \delta\mathbf{d} \in \mathcal{V}_1$, where $\mathcal{U}_1 \subset \mathcal{H}^1(\Omega)$ is the set of kinematically admissible functions, $\mathcal{V}_1 \subset \mathcal{H}^1(\Omega)$ is the spaces of admissible variation fields, and \mathcal{H}^1 is the Hilbert space of order one, in which only the functions that, together with their derivatives up to first order, are Lebesgue square integrable are present. The kinematic boundary conditions are $\mathbf{d} = \bar{\mathbf{d}}$, where $\bar{\mathbf{d}}$ are prescribed displacement and rotation values.

The discretization is performed on element level by approximating the displacement field $\mathbf{d}(x,y)$ by $\mathbf{d} = \bar{\mathbf{N}}(x,y)\mathbf{d}^e$, where \mathbf{d}^e is the vector containing the element degrees of freedom and $\bar{\mathbf{N}}(x,y)$ is the matrix of approximation functions. The deformations of the middle surface are discretized from (16)–(17), which result in

$$\begin{Bmatrix} \boldsymbol{\varepsilon}^o \\ \boldsymbol{\kappa} \end{Bmatrix} = \begin{bmatrix} \mathbf{B}^o \\ \mathbf{B}^b \end{bmatrix} \mathbf{d}^e \quad \text{and} \quad \boldsymbol{\gamma}_c = \mathbf{B}^s \mathbf{d}^e \quad (23)$$

where \mathbf{B}^o , \mathbf{B}^b and \mathbf{B}^s are the membrane, bending and transverse shear strain matrices, respectively, given by

$$\begin{Bmatrix} \mathbf{B}^o \\ \mathbf{B}^b \end{Bmatrix} = \begin{bmatrix} \mathbf{L}^o \bar{\mathbf{N}} \\ \mathbf{L}^b \bar{\mathbf{N}} \end{bmatrix} \quad \text{and} \quad \mathbf{B}^s = \mathbf{L}^s \bar{\mathbf{N}}.$$

The element stiffness matrix is evaluated in the standard way by

$$\mathbf{K}^e = \iiint \left\{ \begin{bmatrix} \mathbf{B}^o \\ \mathbf{B}^b \end{bmatrix}^T \begin{bmatrix} \mathbf{A} & \mathbf{B} \\ \mathbf{B} & \mathbf{D} \end{bmatrix} \begin{bmatrix} \mathbf{B}^o \\ \mathbf{B}^b \end{bmatrix} + \mathbf{B}^{sT} \mathbf{E} \mathbf{B}^s \right\} J d\xi d\eta \quad (24)$$

where J stands for the Jacobian determinant. After superposing the element stiffness matrices and consistent element load vectors, the equilibrium equations for static problems reduces to the standard form $\mathbf{K}\bar{\mathbf{u}} = \mathbf{f}$, where \mathbf{K} is the global stiffness matrix, $\bar{\mathbf{u}}$ is the global degrees of freedom vector and \mathbf{f} is the equivalent nodal load vector. After solving for $\bar{\mathbf{u}}$, one can compute displacements, strain, stresses and resultant forces and moments. Low-order elements can experience shear locking, and thus some strategy must be used to circumvent it. In the applications shown here, none of them was

utilized, and both terms in the element stiffness matrix, membrane-bending, and transverse shear stiffness parts are equally integrated with the same quadrature.

3.2. Stress computation

In this subsection three procedures to compute transverse shear stresses are described: two of them are usual (by constitutive relation and by integration) and the third is a procedure proposed to improve the computed transverse shear stresses.

3.2.1. Procedure 1—shear stresses by the constitutive equations

The transverse shear stress can be directly computed from the shear stress–strain relationship for an arbitrary layer, k , i.e., $\tau_s = \mathbf{C}_s \gamma_s$, where the shear strains γ_s are computed from the GFEM nodal values of displacements using (23).

3.2.2. Procedure 2—shear stresses by integration of the local equilibrium equations

It is observed, however, that the transverse shear stresses obtained from the Mindlin plate model with the constitutive equations are too poor to be useful, since the kinematic model approximates the transverse shear deformation as a constant throughout the thickness of the laminate (see (16) and [54]). As consequences, the correct boundary shear conditions at the faces of the plate are not satisfied, and the model presents errors in shear stresses in non-thin laminates which are too large to be utilized. Thus, the most popular procedure to extract these stresses is the transverse integration of the local differential equilibrium equations for forces which, in the x and y directions and in the absence of body forces, are

$$\begin{aligned} \frac{\partial \sigma_x}{\partial x} + \frac{\partial \tau_{xy}}{\partial y} + \frac{\partial \tau_{xz}}{\partial z} &= 0 \\ \frac{\partial \tau_{xy}}{\partial x} + \frac{\partial \sigma_y}{\partial y} + \frac{\partial \tau_{yz}}{\partial z} &= 0 \end{aligned} \quad (25)$$

Expressions for the x and y differentiation of \mathbf{B}^o and \mathbf{B}^b are analytically obtained from their definitions, such that the left equation in (23) can be differentiated and derivatives of $\boldsymbol{\varepsilon}^o$ and $\boldsymbol{\kappa}$ can be computed. Next, derivatives of the in-plane stresses in an arbitrary position z within each layer k are computed from

$$\begin{aligned} \frac{\partial \boldsymbol{\sigma}}{\partial x} &= \mathbf{Q}^k \left\{ \frac{\partial \boldsymbol{\varepsilon}^o}{\partial x} + z \frac{\partial \boldsymbol{\kappa}}{\partial x} \right\} \\ \frac{\partial \boldsymbol{\sigma}}{\partial y} &= \mathbf{Q}^k \left\{ \frac{\partial \boldsymbol{\varepsilon}^o}{\partial y} + z \frac{\partial \boldsymbol{\kappa}}{\partial y} \right\} \end{aligned} \quad (26)$$

The shear stress estimate is obtained by integrating each one of the equations in (25), using the derivatives of the in-plane stresses in (26), and applying the boundary conditions $\tau_{xz}(x, y, z = -t/2) = \tau_{yz}(x, y, z = -t/2) = 0$. For the first equation, e.g. the stresses in a coordinate z within a layer k , are given by

$$\tau_{xz}^k(\mathbf{x}, z) = \tau_{xz}^k(\mathbf{x}, z_{k-1}) - \int_{z=z_{k-1}}^z (\sigma_{x,x} + \tau_{xy,y}) dz \quad (27)$$

for $z_{k-1} \leq z \leq z_k$, where $\mathbf{x} = (x, y)$, z_{k-1} and z_k are the z coordinates of the lower and upper surfaces of the layer k . As usual, the layer numbering begins at the “lower” surface of the laminate ($z_0 = -t/2$) moving toward the top ($z_N = t/2$). The integration is performed layer by layer, beginning with the first one, and the following continuity conditions are applied at the layer interfaces: $\tau_{xz}^k(x, y, z_{k-1}) = \tau_{xz}^{k-1}(x, y, z_{k-1})$ and $\tau_{yz}^k(x, y, z_{k-1}) = \tau_{yz}^{k-1}(x, y, z_{k-1})$.

3.2.3. Procedure 3—correction of the shear stresses

From (27), it is clear that, in order to obtain accurate transverse shear stresses from integration, it is essential to obtain not only accurate in-plane stresses but also their x and y derivatives. This should require accurate second derivatives of the displacements. On the other hand, the transverse shear stresses obtained directly from the constitutive relations require only good first derivatives of the displacements. They are, therefore, one order more accurate (when compared to the analytic solution also obtained from constitutive equations), than the responses obtained from integration.

The process of integration of the local differential equilibrium equations incorporates physical information on the system, regarding the stress variation through the thickness, but is dependent on an accurate description of the in-plane stresses along the surface. With this in mind, a third and simple procedure can be proposed to improve the integrated transverse shear stresses, appropriate for the FEM with high-order basis functions, such as those provided by GFEM. This procedure is summarized in the following steps for an arbitrary point (x, y) :

- (i) Compute the transverse shear stresses from constitutive equations (τ_{xz} and τ_{yz}) at discrete points p_j through the thickness of each layer.
- (ii) Compute the transverse shear stresses by integration of the equilibrium equations (τ_{xz}^i and τ_{yz}^i) at discrete points p_j through the thickness of each layer.
- (iii) Compute the transverse shear forces from the constitutive shear stresses

$$Q_x = \int_{z=-t/2}^{t/2} \tau_{xz} dz, \quad Q_y = \int_{z=-t/2}^{t/2} \tau_{yz} dz \quad (28)$$

In fact, Q_x and Q_y can also be computed directly from the constitutive relations of the laminate.

- (iv) Compute the transverse shear forces from the integrated shear stresses

$$Q_x^i = \int_{z=-t/2}^{t/2} \tau_{xz}^i dz, \quad Q_y^i = \int_{z=-t/2}^{t/2} \tau_{yz}^i dz \quad (29)$$

- (v) Compute the correction factors

$$R_x = \frac{Q_x}{Q_x^i}, \quad R_y = \frac{Q_y}{Q_y^i} \quad (30)$$

- (vi) Compute the corrected discrete values of stresses by

$$\tau_{xz}^c = R_x \tau_{xz}^i, \quad \tau_{yz}^c = R_y \tau_{yz}^i \quad (31)$$

In this process, if the constitutive values are computed accurately, they can be used to provide reliable constant values Q_x and Q_y at the (x, y) point, while the variation through the thickness is provided by the physical input of the local equilibrium equation. It must be observed that this procedure is heuristic, in the same sense as the widely used post-processing of the shear stresses by integration of the local equilibrium equations.

4. Numerical results

Some aspects of the behavior of the present formulation, when applied to the bending of Mindlin laminated plates, are tested for the typical problem of a square symmetric laminate. Numerical values are compared with the analytical solution obtained for the problem, also under the Mindlin hypothesis, according to [55]. The aspects investigated are the following: (a) First, the integrability of the element matrices is considered. A crude attempt is made to identify the appropriate number of integration points. In order to reduce the number of parameters involved, this analysis

is first performed only on a regular mesh. Different cloud edge functions are tested, the exponential and polynomial ones, always generating approximation functions with C^1 continuity or higher. This is aimed at obtaining stress approximations with inter-element continuity. Also, within this framework, the transverse shear stresses are extracted with the integration of equilibrium equations. The effect of *thickness ratio* (length/thickness) on the response is also evaluated for several degrees of polynomial enrichment. (b) The second part of the analysis is an evaluation of the effect of severe mesh distortions on the accuracy of the response for different laminate thicknesses and enrichment degrees.

In all cases, two measurements of response are used. The first one is the ratio E/E_0 between the *energy of deformation* of approximated response, E , and of the analytical response, E_0 . The second measurement is the *relative error*, defined as

$$e = \sqrt{\frac{E_0 - E}{E_0}} \quad (32)$$

Intrinsic to the Mindlin model is the requirement for a shear factor k_s in the transverse shear constitutive relation. This study does not aim to evaluate its effect and thus a factor $k_s = 1$ is used throughout the computations, either approximate or analytical.

The particular form of the PoU, $\{\phi_x(\mathbf{x})\}$, used in C^k -GFEM is only capable of representing reliably a uniform displacement field. Therefore, a uniform deformation field requires approximation functions ϕ_x^z enriched at least with linear functions, which is the first useful set of enrichment functions (see (9)), although its results show the usual stiffening tendency as the laminate thickness tends to zero. Linear approximations of in-plane deformations require quadratic enrichment, and linear approximations of the transverse shear stresses, obtained by a post-processing of the solution, require cubic enrichment because it involves differentiation of the in-plane stresses.

The present formulation is numerically implemented on partitions of the plate domain in triangular elements with three nodes and straight edges.

Regular meshes composed of equilateral or rectangular triangles have all clouds defined by convex edges, such that the weight functions are obtained with Edwards' scheme. In cases where the exponential cloud edge function is used, all approximation functions generated in the model are C^∞ functions.

However, in most non-structured meshes there will be clouds defined with a mixture of convex and non-convex edges, such that a given weight function can be generated from a product involving, simultaneously, both types of cloud edge functions, those adequate for the convex edges and those for the non-convex ones. Therefore, typically, a given mesh will be modeled with several different types of approximating functions, in each region of the mesh: some clouds will be "pure", with all cloud edge functions "convex", and other clouds, generally most of them, will

have one, two or more pairs of edges whose cloud edge functions are of the type "non-convex". Since the weight function is given basically by a product of several edge functions, many different types of weight functions can be generated, depending on the number of "convex" and "non-convex" edge functions used to define it. One of the consequences is that, in distorted meshes, C^∞ continuity cannot usually be reached everywhere in the mesh. The continuity will be limited to C^k , with k defined by the non-convex cloud edge function chosen. However, even in this case, the limitation of C^k continuity will occur only at the vertices between pairs of non-convex edges [46].

4.1. Numerical applications

The problem considered consists of a simply supported square plate with sides of length $a=b$, thickness t and three equal orthotropic layers with orientations $[0^\circ/90^\circ/0^\circ]$ with respect to axis x . Each layer has the following properties in its orthotropic directions: $E_1 = 25E_2$, $G_{12} = G_{13} = 0.5E_2$, $G_{23} = 0.2E_2$, $E_2 = 7$ GPa and $\nu_{12} = \nu_{23} = 0.25$. A transverse distributed load is applied, defined as $q(x,y) = q_0 \sin(\pi x/a) \sin(\pi y/b)$. The analytical central displacement in the plate, w_0 , is given by [55], and the energy of deformation is $E_0 = q_0 w_0 ab/4$.

The uniform meshes are identified by an index M , which is the number of elements in each direction, as illustrated in Fig. 4 for $M=1$ and 4. In all cases the entire plate is meshed in order to be able to test the coarsest mesh, with $M=1$.

A symmetric laminate is chosen because a pure bending problem is sufficient to highlight all the aspects of interest in the present analysis. This particular configuration also has the advantage of having analytical solutions for the kinematic models of Kirchhoff, Mindlin and the higher-order shear deformation theory of Reddy [56], and also possess a full three-dimensional elastic solution by Pagano [57]. Nevertheless, the formulation investigated in this paper is general for arbitrary anisotropic laminates.

The applied simply supported boundary conditions are represented as

For $\mathbf{x} \in \Gamma$, and $x = \text{const}$.

$$\rightarrow u^0(\mathbf{x}) = v^0(\mathbf{x}) = w(\mathbf{x}) = \psi_y(\mathbf{x}) = 0 \quad (33)$$

For $\mathbf{x} \in \Gamma$, and $y = \text{const}$.

$$\rightarrow u^0(\mathbf{x}) = v^0(\mathbf{x}) = w(\mathbf{x}) = \psi_x(\mathbf{x}) = 0 \quad (34)$$

The above conditions for u^0 and v^0 are included for the sake of completeness, since the particular problem being solved is uncoupled and the in-plane displacements vanish everywhere. The imposition of boundary conditions on edges not parallel to the axis, as well as for curvilinear edges, can be dealt with modifications on the PoU functions defined on the edges or with

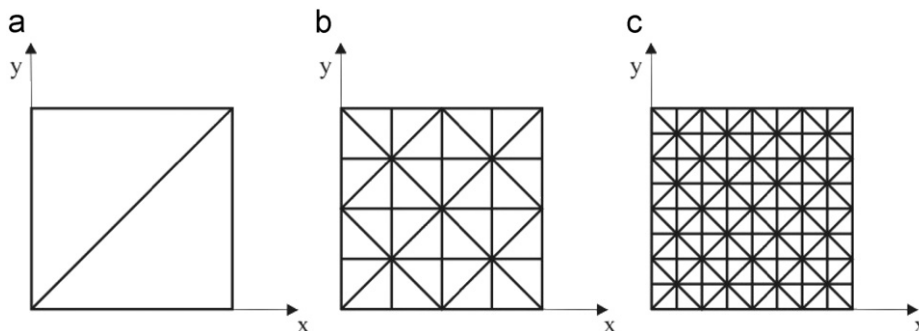


Fig. 4. Examples of meshes used in the laminated plate problem, with mesh indices $M=1$, 4 and 8, and coordinate axis.

procedures similar to those used in, e.g. *hp*-cloud method. These details of the formulation is left for a forthcoming publication.

The actual nodal degrees of freedom to be restricted in order to satisfy conditions (34) can be identified by expressing the complete expression for any of the displacement functions associated with an arbitrary node α , for the partition of unity $\varphi = \varphi(x,y)$ enriched by the fourth degree polynomial (from (9)): taking $w(x, y)$ for example one has

$$w(x,y) = w_1\varphi + w_2(\bar{x}\varphi) + w_3(\bar{y}\varphi) + w_4(\bar{x}^2\varphi) + w_5(\bar{x}\bar{y}\varphi) + w_6(\bar{y}^2\varphi) + w_7(\bar{x}^3\varphi) + w_8(\bar{x}^2\bar{y}\varphi) + w_9(\bar{x}\bar{y}^2\varphi) + w_{10}(\bar{y}^3\varphi) + w_{11}(\bar{x}^4\varphi) + w_{12}(\bar{x}^3\bar{y}\varphi) + w_{13}(\bar{x}^2\bar{y}^2\varphi) + w_{14}(\bar{x}\bar{y}^3\varphi) + w_{15}(\bar{y}^4\varphi) \quad (35)$$

Thus, $w(x, y)$ is defined by the 15 nodal coefficients $w_j, j=1, \dots, 15$, if the PoU is enriched by the fourth degree polynomial. In general, the number of coefficients in (35) are 3, 6, 10 and 15, for uniform enrichment degrees of 1, 2, 3 and 4, according to (9). Since the PoU and the enriched functions are non-dimensional and normalized, and the later are null at the nodes, it follows that the coefficient w_1 (associated with the PoU) is the nodal value of the function $w(x, y)$. The remaining coefficients do not possess a clear physical meaning, although it can be shown that some of them are related to the derivatives of w at the cloud node.

For nodes on boundary lines $x=const.$, one has $\bar{x}=0$, and condition $w=0$ makes it necessary to impose

$$w_1 = w_3 = w_6 = w_{10} = w_{15} = 0 \quad (36)$$

and, similarly, for nodes on boundary lines $y=const.$, one has $\bar{y}=0$ and it is necessary to impose

$$w_1 = w_2 = w_4 = w_7 = w_{11} = 0 \quad (37)$$

The indices are the same for the other displacement functions in (34). One can note that this procedure of selecting nodal coefficients, instead of simply deleting all of the coefficients of the node, enables the interior of the domain to remain enriched, with the monomials involving the coordinate normal to the boundary. For example, in boundaries $x=const.$, monomials in \bar{x} are kept, i.e., those corresponding to coefficients 2, 4, 5, 7–9, 11–14 in (35). Similarly, in boundaries $y=const.$, all monomials in \bar{y} remain: 3, 5, 6, 8–10, 12–15.

It is implied in the concept of a simply supported boundary that $w=0$ not only at the nodes but also along the whole corresponding segment of the boundary. It can be verified that conditions (37)–(38) are sufficient to nullify w along the entire segment of the cloud boundary. This condition can also be

represented by $w = \partial^n w / \partial y^n = 0$, for $n=1,2,\dots$, along a boundary $x=const.$ Differentiation of (35) shows that this is accomplished under the same conditions (36).

4.2. Integrability

The PoU functions generated by the present procedure have complex shapes with large plateaus and sharp hills, as shown in Fig. 12 and also in [39], such that the first and highest derivatives are still more irregular in shape. As a consequence, the coefficients in the stiffness matrix require a considerable amount of computational effort to be integrated. The results shown in Figs. 5–7 consist of the energy ratios versus the number of integration points in order to indicate the minimum amount of integration points necessary to adequately perform the integration in the C^k -GFEM. Fig. 8 shows a comparison between the effect of the integration for the C^0 -GFEM/XFEM and C^k -GFEM. The parameters used in the evaluation are the following:

- The energy ratio E/E_0 between the energy of deformation of approximate response, E , and of the analytical response, E_0 .
- NIP is defined as the square root of the total number of integration points used in the element. Tests are performed with triangular and Gaussian rules. Clearly the triangular rule [58] is the most efficient choice for integration in a triangular element, but the number of points in the available codes are usually limited. In contrast, the Gaussian rule algorithms are easily extended to an arbitrarily large number of points and can be used when a high accuracy of integration is of interest. In the integrability tests shown in this paper Dunavant's triangular rules [58] are used until NIP=8.54 and higher values of NIP are obtained from the Wandzura rule [59].
- Mesh parameter M defined as the number of partitions along directions x and y (illustrated in Fig. 4). In this section all meshes are regular.
- Thickness ratio, a/t , with a and t being the side and thickness of the plate, respectively.
- Degree of the polynomial enrichment, p .
- Type of edge function, designated in the figures as "Exp" for the exponential function, according to (4), or degree of polynomial edge function P , given in (3) [39].

Figs. 5 and 6 show the energy ratio versus NIP for a very thick plate, with ratio $a/t=4$, for enrichments $p=1,2,3$ and 4, and some

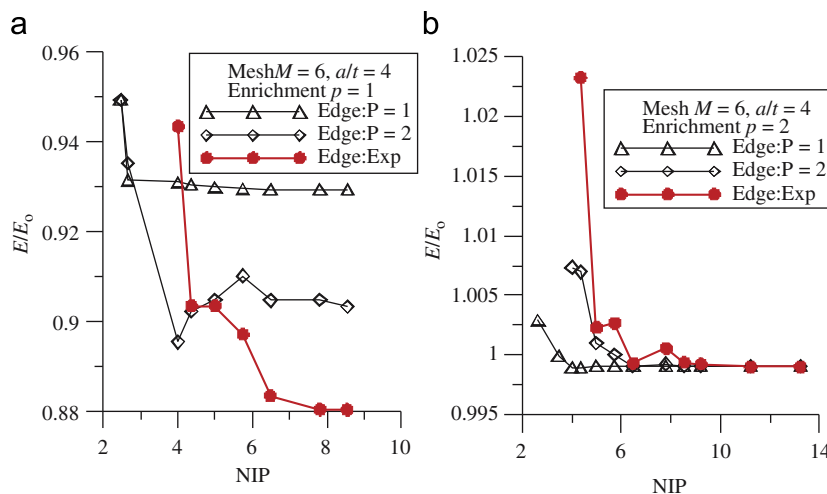


Fig. 5. Energy ratio versus number of integration points (NIP) index for C^k -GFEM with several edge functions, $P=1, P=2$ and exponential, which produce C^0, C^1 and C^∞ partition of unities, respectively. Regular mesh $6 \times 6, a/t=4$. (a) Enrichment $p=1$, (b) $p=2$.

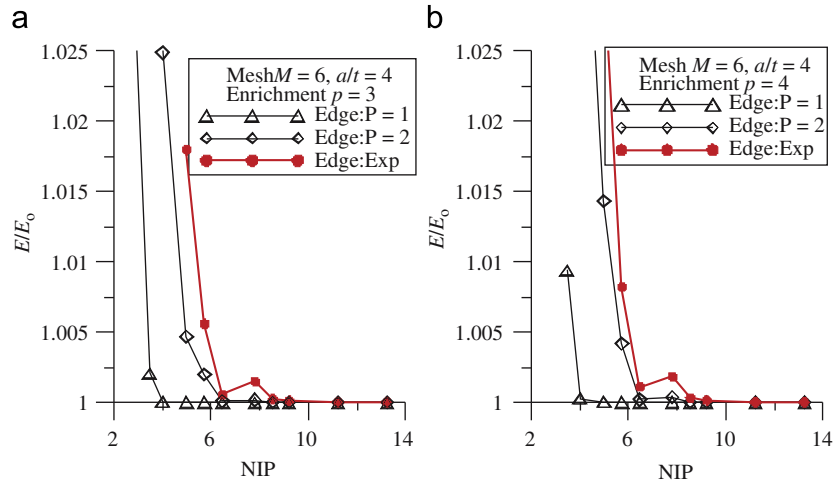


Fig. 6. Energy ratio versus number of integration points (NIP) index for C^k -GFEM with several edge functions, $P=1$, $P=2$ and exponential, which produce C^0 , C^1 and C^∞ partition of unities, respectively. Regular mesh 6×6 , $a/t=4$. (a) Enrichment $p=3$, (b) $p=4$.

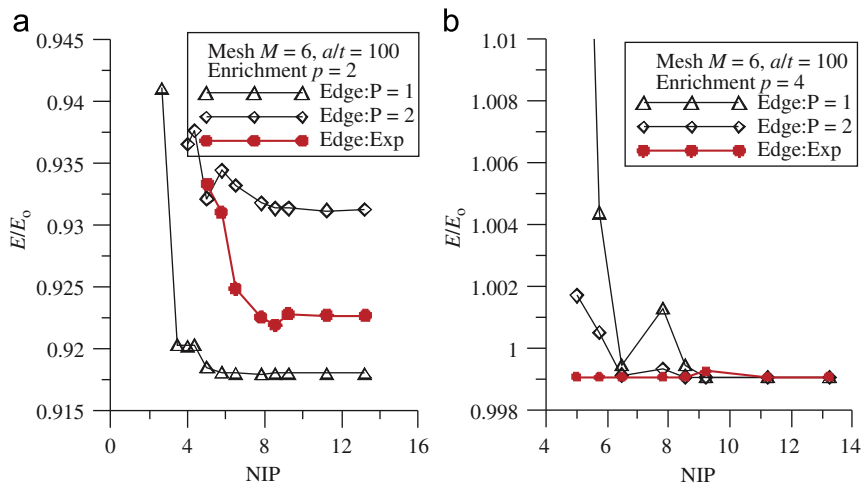


Fig. 7. Energy ratio versus number of integration points (NIP) index for C^k -GFEM with several edge functions, $P=1$, $P=2$ and exponential, which produce C^0 , C^1 and C^∞ partition of unities, respectively. Regular mesh 6×6 , $a/t=100$. (a) Enrichment $p=2$, (b) $p=4$.

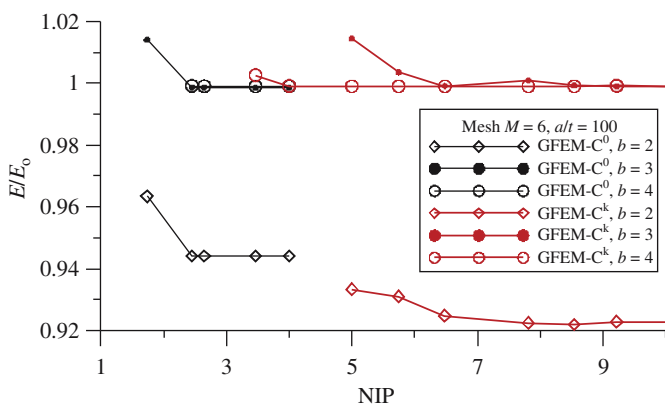


Fig. 8. Energy ratio versus number of integration points (NIP) index for C^k GFEM (with exponential edge functions and C^∞ partition of unity), and C^0 GFEM with linear partition of unity. Mesh 6×6 , basis degree $b=2$, 3 and 4, $a/t=100$, regular mesh 6×6 , triangular integration rule.

different edge functions. Triangular integration rules are used with a fixed mesh $M=6$. Fig. 7 shows similar results for a thin plate with $a/t=100$ and enrichment degrees $p=2$ and

4 respectively.³ In all cases, it can be seen that for a higher degree of the polynomial in the edge function it is more difficult to adequately integrate the element matrices. In general, the edge function of degree $P=1$ is the most easily integrated, requiring approximately $NIP=5$. It should be noted that this function leads to C^0 functions only, the least continuity required to the Mindlin model. The most easily integrated configurations with interelement continuous in-plane stresses can be obtained with edge functions of degree $P=2$, which lead to C^1 PoU, or exponential functions, which lead to C^∞ PoU and require similar integration effort, with NIP values of approximately 6.48–8.

Fig. 8 shows a comparison between the energy ratio versus the number of integration points (NIP) index for: (a) the present formulation, C^k -GFEM (with exponential cloud edge functions and, therefore, C^∞ partition of unity) and (b) the standard C^0 -GFEM obtained from the linear partition of unity enriched with global

³ Although the Mindlin kinematic model is incapable of accurately predicting response for such thick plates as $a/t=4$, some results for this case are included here in order to observe the behavior of the numerical procedures in an extreme case, opposite to the other practical extreme, $a/t=100$. This is usual, since we are investigating the behavior of the numerical approximation procedures, rather than the efficiency of the kinematic model.

polynomials of degree p . Results are shown with reference to b , the degree of the basis in the element. For the C^k -GFEM, $b=p$, since the C^k partition of unity can only reliably represent a constant displacement field. On the other hand, the partition of unity used in C^0 -GFEM is built with the linear tent functions. Therefore, when it is enriched with polynomials of degree p , the resulting basis is able to span the polynomials of degree $b=p+1$. The results in Fig. 8 show that the C^0 -GFEM is much easier to integrate, requiring around NIP=2.45, while C^k -GFEM requires NIP=4–8.

Some of the numerical data used to generate the curves in Figs. 5–8 were used to compute the relative error $e_{15} = (E - E_{15})/E_{15}$, as shown in Table 1, where E_{15} is the energy of the numerical solution obtained with NIP=15. Therefore, e_{15} is not the solution error, but an estimative of the relative error of the integration. The table shows this error for NIP=9 and 12, for all polynomial degrees of enrichment tested, for cloud edge functions $P=2$ and exponential, and thickness ratios $a/t=4$ and 100. The results show that the thick laminate is easier to integrate than the thin one, for both edge functions, if the enrichment function degree is $p=2$. On the other hand, the results for enrichments $p=3$ and 4 show the opposite case, i.e., the thin configuration is easier to integrate.

Fig. 9 shows the variation in the energy ratio with mesh index, M , for different enrichment functions and thicknesses $a/t=4$ and 100. The edge function is exponential, which produces C^∞ partition of unity, and the triangular integration rule with NIP=6.48 is used. The results for the thin laminate with enrichment $p=1$ are excessively stiff to be shown with the other results in the same graph and are omitted, as expected due to locking. The entire set of curves show smooth, monotonic convergence for all enrichments and both laminate thicknesses.

Table 1
Variation of the relative error in energy, $(E - E_{15})/E_{15}$, with thickness ratio a/t , for C^k -GFEM. Cloud edge functions $P=2$ and exponential, which lead to C^1 and C^∞ partition of unities, respectively. Gaussian rule with NIP=9 and 12 and mesh index $M=6$. Values are multiplied by 10^6 .

a/t	4		4		100		100	
	Edge function	NIP						
1	$P=2$	9	$P=2$	12	Exp	9	Exp	12
2	$P=2$	9	$P=2$	12	Exp	9	Exp	12
3	$P=2$	9	$P=2$	12	Exp	9	Exp	12
4	$P=2$	9	$P=2$	12	Exp	9	Exp	12

a/t	4	4	4	4	100	100	100	100
Edge function	$P=2$	$P=2$	Exp	Exp	$P=2$	$P=2$	Exp	Exp
p	NIP							
	9	12	9	12	9	12	9	12
1	706	84.7	3460	426				
2	29.7	19.4	-61.8	30.7	315	39.0	1740	-23.9
3	36.8	2.83	174	6.32	4.01	0.694	-21.0	11.0
4	91.2	1.03	292	7.96	6.04	0.092	42.3	1.15

The thickness effect can be seen in Fig. 10, where the error is given in terms of the relative error e . The edge function chosen is exponential, which, accordingly to the previous results, requires more integration points than the polynomial ones. The Gaussian rule with NIP=20 is applied in order to evaluate the errors with sufficient accuracy and the mesh index is $M=6$. Results range from $a/t=4$ to 1000. This shows the sensitivity of the results with respect to the thickness, for all enrichments considered, although no sharp stiffening peak was observed in any computations.

4.3. Mesh distortion test

Fig. 11 shows some distorted meshes which are generated starting from a regular mesh of 2×2 and 4×4 elements and

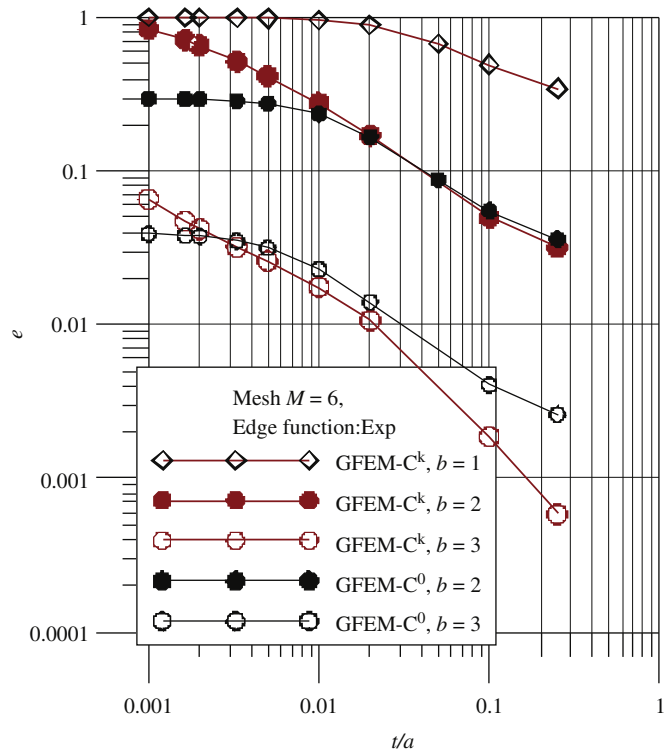


Fig. 10. Relative error $e = \sqrt{(E_0 - E)/E_0}$ versus thickness ratio t/a for different enrichment functions p . Exponential edge function and C^∞ partition of unity, triangular integration rule with NIP=13.23. Regular mesh 6×6 .

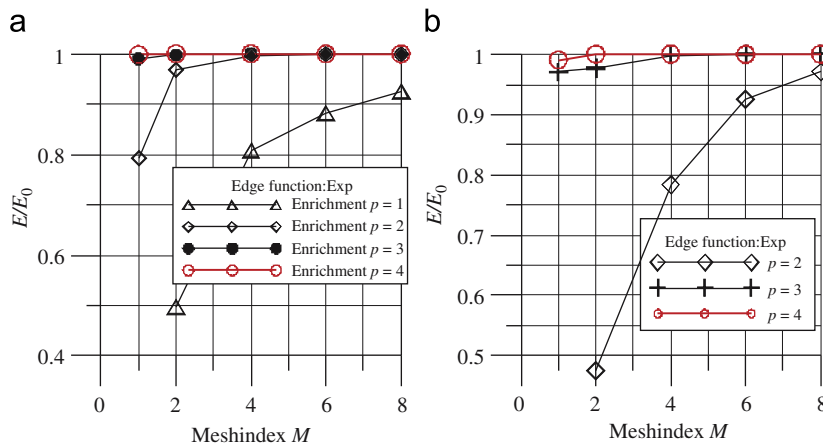


Fig. 9. Energy ratio for different mesh indices M and enrichment functions p , for C^k -GFEM with C^∞ partition of unity. Triangular rule with NIP=6.48. (a) $a/t=4$, (b) $a/t=100$.

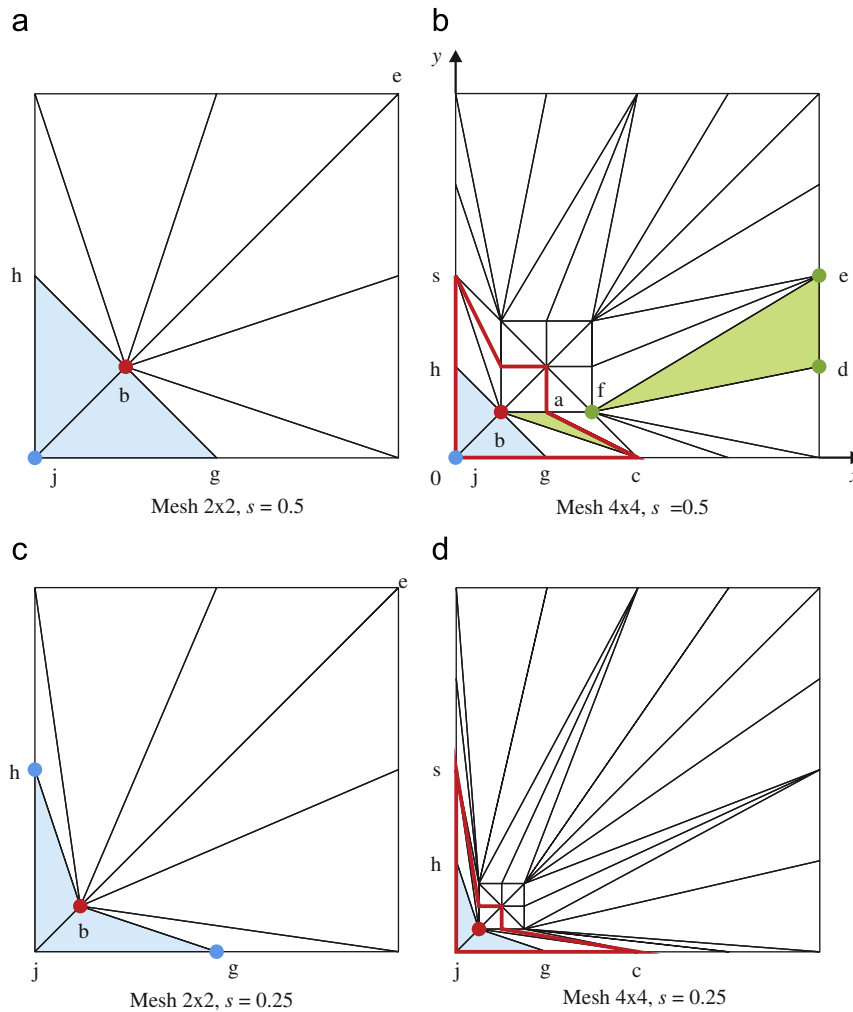


Fig. 11. Illustration of some distorted meshes, with cases of convex and non-convex edges and coordinate axes. (For interpretation of the references to color in this figure legend, the reader is referred to the web version of this article.)

multiplying the coordinates of the internal nodes by a constant s , such that $s \in (0; 1]$. The parameter $s=1$ indicates a regular mesh, examples of which are given in Fig. 4. For the mesh 2×2 , in Fig. 11(a), all clouds are defined by convex edges for $s \geq 0.5$, and all approximation functions can be chosen to be C^∞ . For $0 < s < 0.5$, as in Fig. 11(c), the cloud of node j , formed by nodes $jgbh$, has non-convex gb and bh edges, such that the weight function associated with node j will have limited continuity at the node b . Figs. 12(a) and (c) show the PoU function associated with this node corresponding to the meshes in Figs. 11(a) and (c), respectively. In all results the edge functions on convex edges are exponential, and on non-convex edges they are obtained from (7) with $k=4$. Although the functions displayed in both figures have different natures and continuities, their general aspect is similar. For $s=0.25$ the node b is closer to corner j than in the case $s=0.5$, such that the function becomes steeper from 0 to 1, with a larger gradient between the two nodes. This gradient becomes larger as the parameter s decreases. Along most of the diagonal jb , on the other hand, the function follows a plateau close to unity, in a similar fashion to the functions C^∞ of regular meshes as shown in [39]. The region close to the corner, with large gradients, and the plateau region suggest two distinct regions with different interpolator abilities offered by the PoU function. This difference can be, in principle, equilibrated by the adequate choice of enrichment functions in each region.

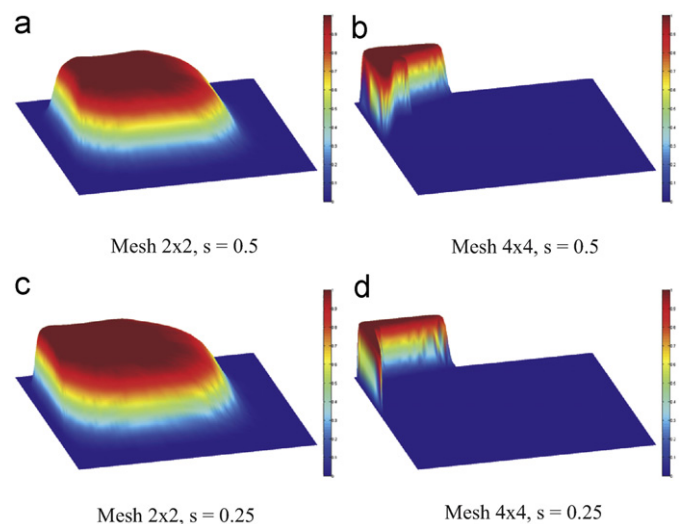


Fig. 12. Views of non-enriched basis functions defined in convex and non-convex edges, for C^k -GFEM.

Figs. 12(b) and (d) show the PoU function associated with node b corresponding to the meshes in Figs. 11(b) and (d) respectively for meshes 4×4 and distortions $s=0.5$ and 0.25 . In contrast to the

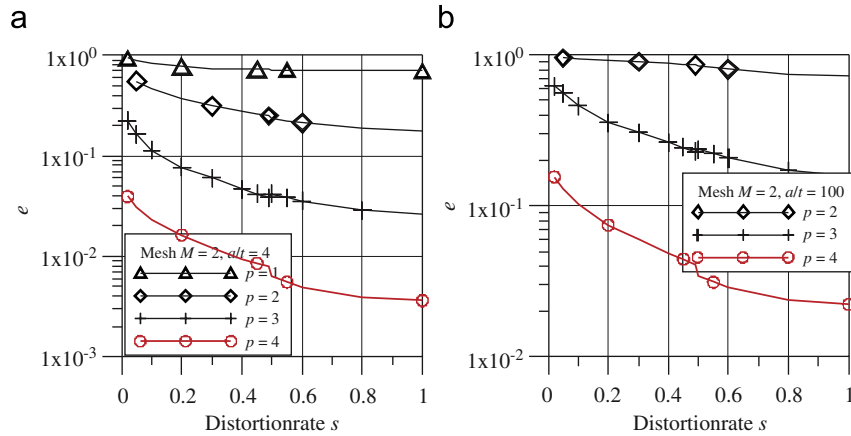


Fig. 13. Mesh distortion test. Error in energy norm, $e = \sqrt{(E_0 - E)/E_0}$ versus mesh distortion ratio, s , for C^k -GFEM. Gaussian rule with NIP=30. Mesh 2×2 , edge function Exp, continuity $k=4$. (a) $a/t=4$, (b) $a/t=100$.

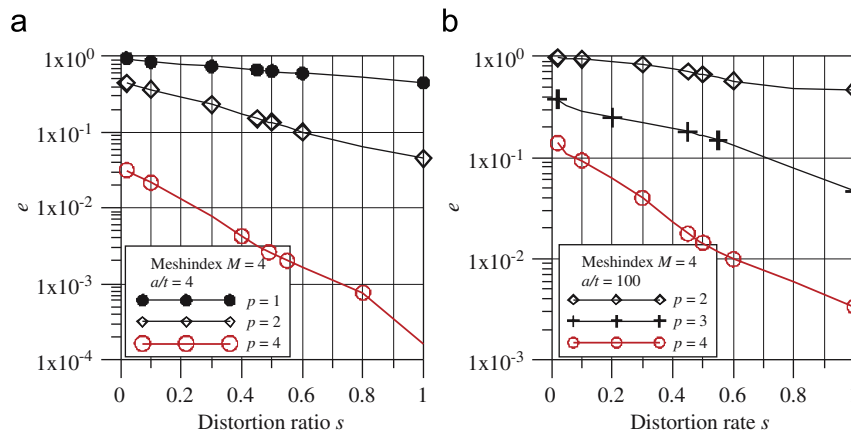


Fig. 14. Test on mesh distortion. Error in energy norm, $e = \sqrt{(E_0 - E)/E_0}$ versus mesh distortion ratio, s , for C^k -GFEM. Gaussian rule with NIP=30. Mesh 4×4 , edge function Exp, continuity $k=1$. (a) $a/t=4$, (b) $a/t=100$.

mesh 2×2 , here there is no amount of distortion that can result in a pure mesh with all functions C^∞ . The cloud j , formed by nodes $jgbh$, are convex for $s \geq 0.5$, as in Fig. 11(b), and non-convex for $s < 0.5$, as in the Fig. 11(d), where the edges gbh generate C^k weight functions at node b . On the other hand, the cloud associated with node b , in Figs. 11(b) and (d), marked with red boundaries (line $jasj$), have, for all values of distortion $s < 1$, two concave vertices along the path cas , with two corresponding C^k continuous functions. The functions in Figs. 12(b) and (d) vanish along the edges of the cloud (red line in Figs. 11(b) and (d)), and the gradients near the edges increase considerably as s is reduced.

4.3.1. Results on distorted meshes

The laminate problem is the same as that described in Section 4.1, but the mesh is distorted according to the parameter s . Illustrations of regular and distorted meshes are shown in Figs. 4 and 11, respectively. Fig. 13 shows the error in the energy norm versus distortion, for $M=2$, that is, eight elements on the entire laminate. The plate is thick, with $a/t=4$. The results were obtained with a continuity constant $k=4$ in these functions, and in Fig. 13 the curves were obtained with more points around the value $s=0.5$, in order to identify some discontinuity in the response at the value below which there are non-convex clouds. This discontinuity is more pronounced in the curve for enrichment $p=4$, but can be noted in the other curves as well. For a thin laminate, $a/t=100$, Fig. 13(b) shows similar results as those

obtained for the thick plate, except that results are not obtained for enrichment $p=1$. In both figures, a large number of integration points is used, NIP=30, in order to obtain enough integration accuracy to be able to estimate approximation errors in the energy norm of the order of 10^{-8} , as in the results that follow.

Fig. 14 shows the results for the error versus distortion rate for a mesh $M=4$, of the type shown in Figs. 11(b) and (d). In this mesh there are non-convex clouds for any distortion $s \neq 1$.⁴ Therefore, no discontinuity is seen in the curves, since the types of edge functions are the same for all values of s , except for the undistorted mesh, $s=1$. In all curves, the smallest value of s was arbitrarily chosen as $s=0.02$. The numerical data used to generate Fig. 14(b) (for the very thin laminate) shows that, for enrichments $p=3$ and 4, the errors start to increase quickly as s is reduced to values below 0.06.

Fig. 15 shows the energy ratio versus NIP for different continuity parameters k used in the functions for non-convex edges in a distorted mesh with $s=0.5$ and $M=4$. The edge functions on convex edges are exponential. The laminate is thin, with $a/t=100$. The curves show a slight tendency toward lower values of continuity k being easier to integrate. However,

⁴ For this test, the continuity constant was arbitrated to $k=1$ (differently from Fig. 13), only for the sake of illustrating responses with different values of k . The results for $k=4$ (not shown) are qualitatively similar to these for $k=1$.

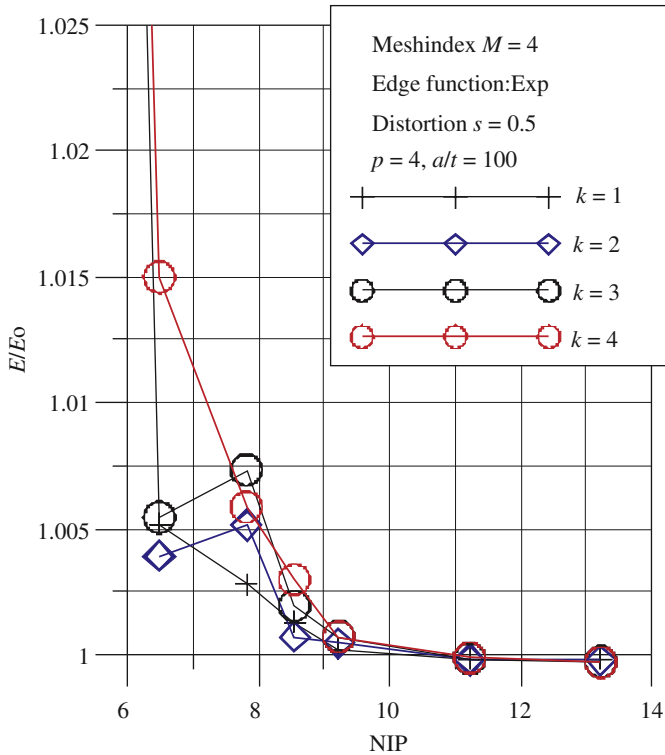


Fig. 15. Test on mesh distortion in C^k -GFEM. Energy ratio versus NIP, for different continuity parameters k . Triangular integration rule. Mesh distortion ratio, $s=0.5$. Mesh 4×4 , edge function Exp, $a/t=100$.

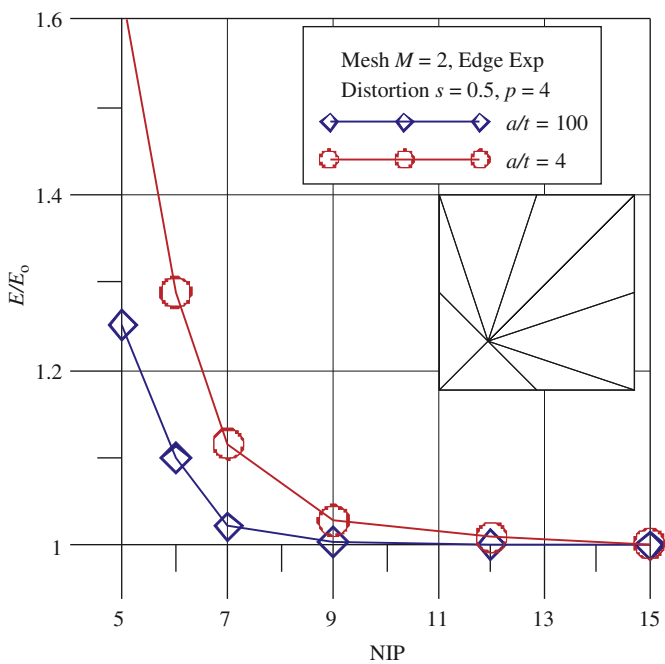


Fig. 16. Test on mesh distortion in C^k -GFEM. Energy ratio versus Gaussian integration rule with NIP, for different thicknesses. Mesh distortion ratio, $s=0.5$. Mesh 4×4 , edge function Exp, $a/t=100$. Continuity $k=4$.

considering an error of about 0.6% as sufficient in a routinely engineering analysis, it can be seen that NIP about 8 is sufficient for any of the k 's tested.

The influence of the thickness on the integration effort is seen in Fig. 16, for $s=0.5$, enrichment $p=4$ and a continuity constant $k=4$ for the non-convex edges. In this case the Gaussian rule is

used. While for $a/t=100$ integration requires an NIP of 9–10, for $a/t=4$ more points are needed, around 12 or 13. As is normally the case, the results obtained by applying the Gaussian rule are monotonic, in contrast to most of those obtained by applying the triangular rule.

A general comparison between the behavior of the mesh distortion of the present continuous formulation, C^k -GFEM, and the standard C^0 -GFEM can be seen in Fig. 17, with the relative error e versus the distortion ratio s for different basis degrees b . For the C^k -GFEM, $b=p$, and for C^0 -GFEM, $b=p+1$, where p is the degree of the enrichment. The edge function is exponential and the continuity parameter is $k=1$. Gaussian integration with NIP=30 was used. One can observe that for basis degrees 3 and 4 the continuous formulation is more accurate for all levels of distortion and for degree 2 the results are similar to those of the C^0 formulation.

It should be pointed out that, for the same order b , the number of degrees of freedom is different between both formulations, and the C^k -GFEM involves more operations to perform the analysis, although, with smaller errors, depending on the basis degree and the level of mesh distortions.

The mesh distortion parameter s can be related to other geometrical parameters associated with the mesh distortion. Let us consider the mesh $M=4$, under an arbitrary distortion s , as shown in Fig. 11(b) or (d). As s is reduced, an element like the one denoted by nodes abc , tends to distort a straight triangle into a needle-like shape. The aspect ratio of this element can be determined as follows. Considering a Cartesian coordinate system with the origin at node j , and a square plate of sides a , one can identify the following coordinates for nodes a, b and c :

$$\begin{aligned} \mathbf{x}_a &= (x_a; y_a) = \frac{as}{4} (2; 1) \\ \mathbf{x}_b &= (x_b; y_b) = \frac{as}{4} (1; 1) \\ \mathbf{x}_c &= (x_c; y_c) = \frac{a}{2} (1; 0) \end{aligned} \quad (38)$$

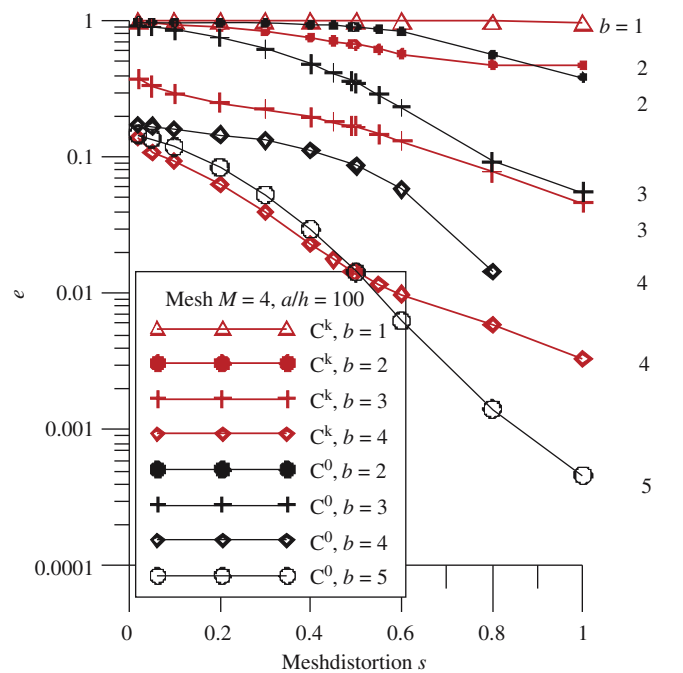


Fig. 17. Error in energy norm e versus distortion ratio s for different basis degrees b , for GFEM- C^k and GFEM- C^0 . Edge function Exp, continuity parameter $k=1$, Gaussian integration with NIP=30.

The vectors along the sides ca and cb are $\mathbf{v}_a = \mathbf{x}_a - \mathbf{x}_c$ and $\mathbf{v}_b = \mathbf{x}_b - \mathbf{x}_c$. The vector along the height of the triangle abc associated with the base cb is given by $\mathbf{h} = \mathbf{v}_a - (\mathbf{v}_a \cdot \hat{\mathbf{v}}_b)\hat{\mathbf{v}}_b$, where $\hat{\mathbf{v}}_b$ is the unit vector along \mathbf{v}_b . Simplifications show that

$$\|\mathbf{h}\| = \frac{as^2}{4\sqrt{2}\sqrt{2-2s+s^2}}, \quad \|\mathbf{v}_b\| = \frac{as^2\sqrt{2-2s+s^2}}{2\sqrt{2}},$$

such that the aspect ratio of the smallest element becomes

$$r_m \equiv \frac{\|\mathbf{v}_b\|}{\|\mathbf{h}\|} = \frac{2(2-2s+s^2)}{s^2}. \quad (39)$$

The area of element abc is $A_1 = l_{ab}y_b/2$, where $l_{ab} = (x_a - x_b)$ is the distance ab . Simplification gives $A_1 = a^2b^2/32$. The element def in Fig. 11(b), is the largest one in the mesh. Its area is $A_2 = (4-3s)a^2/32$. The following element area ratio is defined as

$$m_m \equiv \frac{A_2}{A_1} = \frac{(4-3s)}{s^2}. \quad (40)$$

Fig. 18 shows the evolution of r_m and m_m with the parameter s used to generate the distorted mesh. Observing Figs. 13 and 14 one can note that the simulation is extended to very small values of s . The extreme value of $s=0.02$ was arbitrarily chosen for the simulations, and all results for this mesh are still “reasonable”, although much less accurate than those for larger values of s . With the help of Fig. 18, one can observe the level of distortion from two other viewpoints. For $s=0.02$, (39) and (40) gives $r_m=9802$ and $m_m=9900$ for mesh $M=4$, i.e., the smallest element

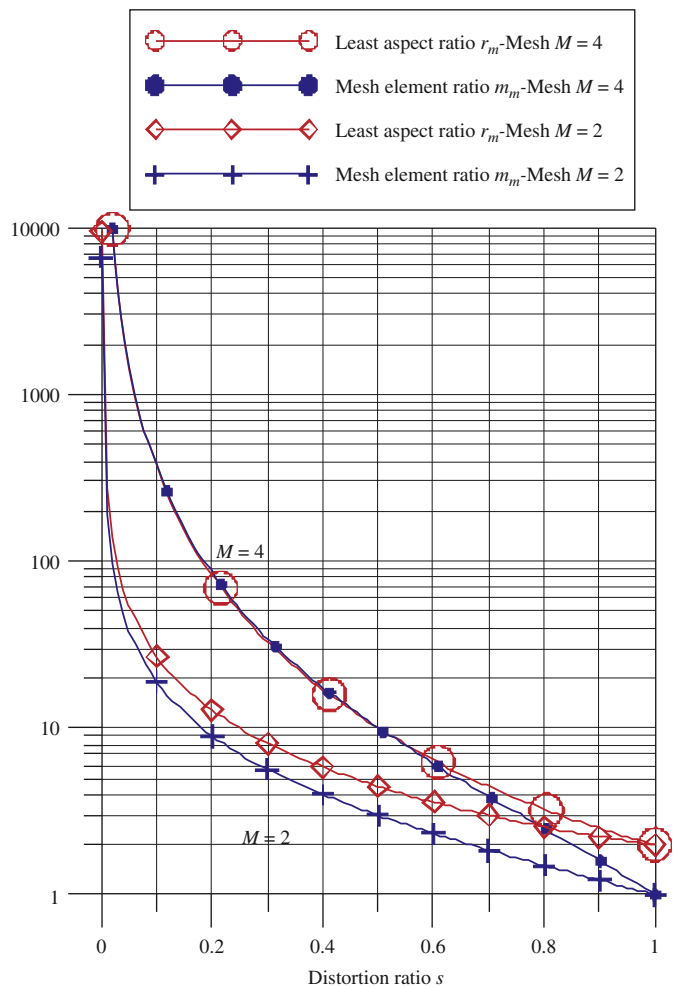


Fig. 18. Variation in the element aspect ratio and element size ratio with distortion ratio for distorted mesh $M=2, 4$.

Table 2 Condition number for continuous and standard GFEM in distorted meshes.

Distortion parameter s	C^k -GFEM	C^0 -GFEM
1.0	9.74	13.4
0.8	10.6	13.5
0.6	13.3	14.6
0.4	16.3	16.5
0.2	20.7	19.0
0.05	26.8	23.8

is a needle with aspect ratio 9802:1 and the ratio between the largest and the smallest element in the mesh is 9900:1. In general, no mesh generator produces such distorted elements although elements with aspect ratios of around 100 can be produced in badly generated geometries, with cusps and other maladies. Other situations where severe distortion occurs, with aspect ratios of around 100, are those generated from the large material deformation in Lagrangian meshes, in processes like metal forming, for example.

4.3.2. Condition number of the stiffness matrix

Table 2 shows the variation in the condition number with the distortion parameter s . The results are obtained from both, smooth C^k -GFEM and the standard C^0 -GFEM formulations. The mesh used is $M=4 \times 4$, and the degree of the most complete polynomial is $b=4$. In the continuous formulation the edge function is exponential, with a continuity parameter $k=1$. In all cases, the integration rule is triangular with NIP=11.2. It can be seen that, for moderate levels of distortion, the smooth C^k -GFEM shows stiffness matrices significantly better conditioned than the standard C^0 -GFEM. However, for more severe distortions, with $s=0.6$ or smaller, the condition number is equally excessive for both formulations.

The high condition numbers for C^0 -GFEM are well known, and it makes necessary the use of the iterative $K-\epsilon$ method [52,60] to solve the algebraic system of equations, irrespective of the mathematical model being discretized. Results like those shown in Table 2, for models with mesh distortion, consistently indicate better condition number with C^k -GFEM.

4.4. Stresses

Some stress distributions along the thickness are presented and discussed as follows. Figs. 19 and 20 show normalized in-plane and transverse shear stresses through thickness at the center of the laminate and at the center of the boundary at the y -axis, $(0;a/2)$, respectively. The exponential edge function and Gaussian integration with NIP=10 for the in-plane stresses and triangular rule with NIP=11.22 for the shear values were used.⁵ The laminate is very thick, with $a/t=4$. Only enrichments $p=1$ and 2 give results sufficiently distant from the analytical curve of σ_x to be visible on the graph, therefore, results for $p=3$ and 4 are not shown. The analytical values for shear stresses shown were obtained by constitutive equations and by integration of the local equilibrium equations, according to (27).

The C^k -GFEM results in Fig. 20 are the transverse shear stresses obtained directly from the constitutive equations, from integration of the local equilibrium equations and corrected values obtained from (28)–(31). These values are indicated as “constitutive”,

⁵ The integrated shear stresses utilize second derivatives, which are more oscillatory than the first derivatives utilized in the in-plane stresses. The triangular rule was chosen for the shear stresses due to its better efficiency in triangular domains, compared with the Gaussian rule. However, the Gaussian rule could be utilized as well.

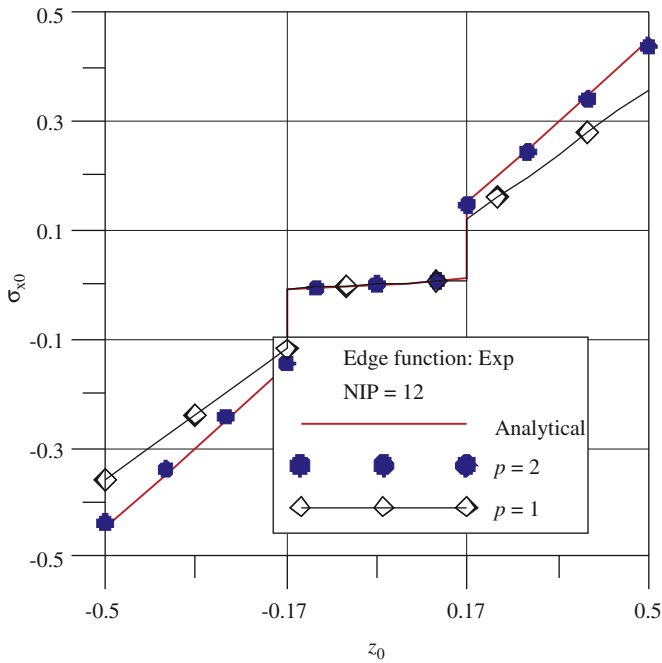


Fig. 19. Normalized in-plane normal stress $\sigma_{x0} = \sigma_x t^2 / (q_0 a^2)$, along the thickness at $(x; y) = (a/2; b/2)$, with C^k -GFEM. Normalized coordinate $z_0 z/t$. Exponential edge function, Gaussian integration rule with NIP=12. $a/t=4$. Mesh index $M=6$.

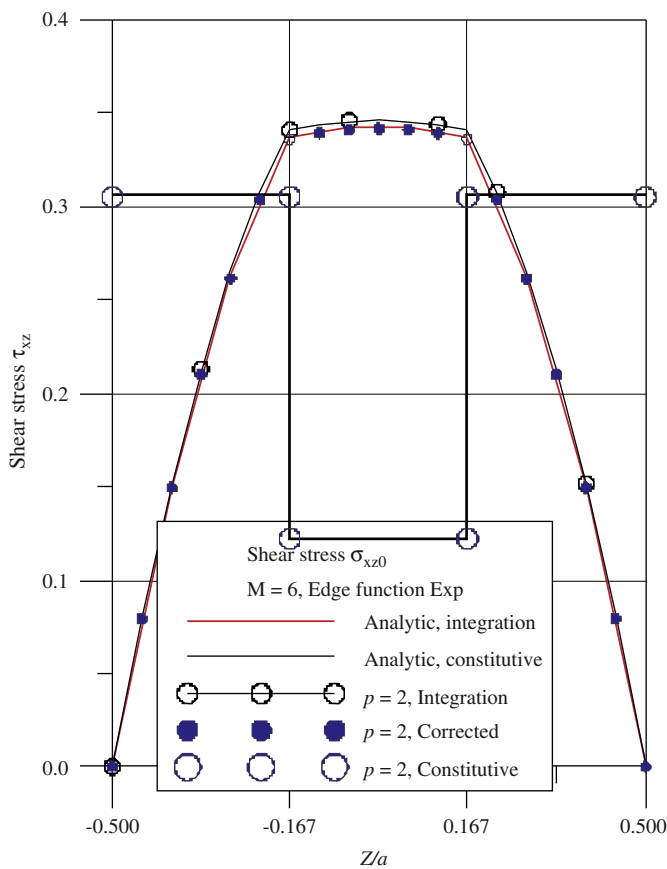


Fig. 20. Normalized transverse shear stress $\tau_{xz0} = \tau_{xz} t / (q_0 a)$, along the thickness at $(x; y) = (0; a/2)$, with C^k -GFEM. Exponential edge function, C^∞ partition of unity, triangular integration rule with NIP=11.22. $a/t=4$. Mesh index $M=6$.

“integration” and “corrected”, respectively. Since the integration procedure requires the differentiation of the approximated in-plane stresses, the least required enrichment is $p=2$. The responses for $p=3$ and 4 become visually indistinguishable on the analytical curve and are not shown. Numerical values are shown in Table 3 for enrichment $p=2$. The accuracy of the shear stresses obtained from the constitutive equations (τ_{xz0}) and the improvement of the corrected values (τ_{xz0}^c) in relation to the integrated ones (τ_{xz0}^i) can be noted.

Fig. 21 shows the transverse shear stress at the reference surface of the laminate versus y -axis, along the boundary $x=0$, for enrichments $p=2$ and 3. One can note that for $p=2$ the integrated approximation is irregular, probably due to intrinsic characteristics of the second derivatives of the C^k -GFEM basis functions. As expected, values for $p=3$ show a smoother variation along the boundary. The same figure also shows the results for the shear stresses obtained from the corrections of (28)–(31). These corrections have the ability to improve and smoothen the curve, even for $p=2$. The irregularities observed in the second derivatives were also shown in the transverse shear stresses, Fig. 24.

4.5. Transverse shear stresses by FEM and C^k -GFEM

In this section the cost of the analysis is appreciated by comparing three methods: the standard FEM, the standard discontinuous C^0 -GFEM and the continuous C^k -GFEM. The problem analyzed is the same square laminated plate used in the previous cases, subjected to the same sine distributed load with a maximum value of 0.001 Pa. The total thickness of the laminate is $t=0.020$ m, such that the aspect ratio is $a/t = 10$. Each

Table 3

Normalized stresses along the thickness: $\sigma_{x0} = \sigma_x t^2 / (q_0 a^2)$ at $(x; y) = (a/2; a/2)$ and $\tau_{xz0} = \tau_{xz} t / (q_0 a)$ at $(x; y) = (0; a/2)$. Mesh index $M=6$, $a/t=4$, enrichment $p=2$.

z	Analytic		C^k -GFEM				
	σ_{x0}	τ_{xz0}	τ_{xz0}^i	σ_{x0}	τ_{xz0}	τ_{xz0}^i	τ_{xz0}^c
0.0	0.0	0.122354	0.342815	0.0	0.1220	0.3465	0.3417
0.167	0.010241	0.122354	0.337052	0.0100	0.1220	0.3410	0.3363
0.167	0.149161	0.305885	0.337052	0.1457	0.3051	0.3410	0.3363
0.500	0.447483	0.305885	0.0	0.4371	0.3051	0.0	0.0

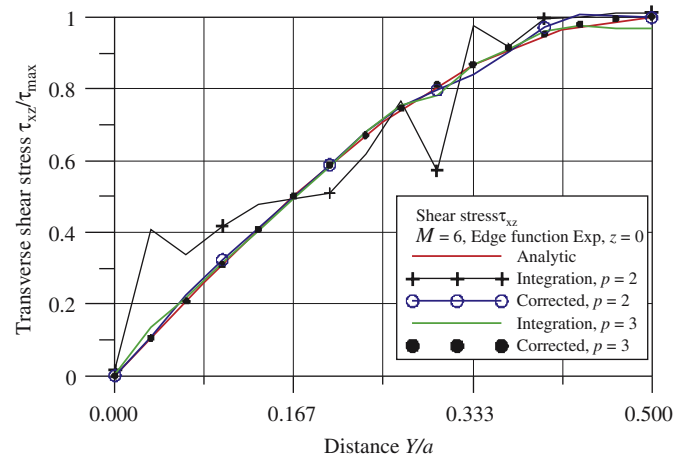


Fig. 21. Normalized transverse shear stress τ_{xz} / τ_{xzmax} versus y/a , along the edge $x=0$ at $z=0$, with C^k -GFEM. Exponential edge function, C^∞ partition of unity, triangular integration rule with NIP=11.22. $a/t=4$. Mesh index $M=6$.

of the three models was designed to have approximately the same number of unrestricted degrees of freedom, so that the computational cost of the solution of the algebraic system of equations is approximately the same in all cases. The characteristics of each model are described next.

1. Standard finite element model. This model was chosen to provide a reference based on the formulations used in most commercial codes. In these codes (see Ansys, for instance), the degenerate solid formulation is used to model shells and plates, which corresponds to a first-order kinematic model. To obtain the results shown here the same first-order model with a triangular element of six nodes and quadratic standard shape functions based on intrinsic triangular coordinates was used. The mesh employed is regular and consists of a grid of 27×27 nodes and 338 triangular elements, rendering 1979 non-restricted degrees of freedom associated with the bending.
2. Standard discontinuous C^0 -GFEM model. The mesh $M=8$ (see Fig. 4), that is, 128 elements and 81 nodes was used. The enrichment functions are of degree $p=3$, such that the basis has degree $b=4$. The number of non-restricted degrees of freedom associated with the bending is 2174.
3. Continuous C^k -GFEM model. The mesh $M=6$ (see Fig. 4), that is, 72 elements and 49 nodes was used. The enrichment functions are of degree $p=4$, such that the basis has degree $b=4$. The edge function is exponential. The number of non-restricted degrees of freedom associated with the bending is 1965.

Table 4 shows the analytical and numerical results for normal stress σ_x at coordinates $(x; y; z) = (a/2; a/2; t/2)$, transverse shear stress at coordinates $(x; y; z) = (0; a/2; 0)$ and energy of deformation E . Transverse shear stress is computed directly from the constitutive equations, τ_{xz} , from integration through the thickness of the local equilibrium equations, τ_{xz}^i , and from the correction procedure from the transverse shear force, τ_{xz}^c . Firstly, observing the energy of deformation, the exceptional accuracy of

Table 4
Energy norm and stresses—comparative results for FEM, C^0 -GFEM and C^k -GFEM. Values multiplied by 1000. Units in J and Pa.

ndof's	Analytical	FEM 1979	C^0 -GFEM 2174	C^k -GFEM 1965
$2E$	1.801674467	1.80142	1.801674457	1.8016787
σ_x	51.7249	51.66	51.721	51.61
τ_{xz}	1.37103	1.385	1.3702	1.3735
τ_{xz}^i	3.82823	3.7368	3.8370	3.8366
τ_{xz}^c			3.8258	3.8352

both forms of GFEM when compared with the standard FEM model can be observed, although in everyday engineering practice the accuracy of the latter is acceptable. The accuracy for the normal stress is similar in all three cases, as in the constitutive transverse shear stress. However, one can note that the relative error in the integrated shear stress for the FEM model is -2.4% , and for GFEM, $+0.23\%$. Considering the corrected values, the C^0 -GFEM relative error is -0.0063% . The explanation for these results is that the process of integration of the equilibrium equations involves differentiation of the in-plane stresses. Therefore, formulations with a low-order basis like the standard FEM used in commercial packages cannot provide accurate integrated values for the transverse shear stresses with the ease the GFEM can provide.

In this section a comparison is made among FEM with quadratic approximation, and C^0 -GFEM and C^k -GFEM with quartic approximations, utilizing one different mesh for each case, in order to obtain approximately the same number of degrees of freedom in each model. The fact that the rate of p -convergence in FEM and GFEM is higher than the rate of h -convergence, apparently renders the present comparison unfair. However, the comparison illustrates perfectly an important part of everyday reality: the FEM formulations most commonly utilized are of low-order basis. Therefore, it shows not only poorer convergence rates, but also, in the case anisotropic laminate bending models, it is unable to provide accurate response to transverse shear stresses (or any other post-processed values that requires higher-order differentiation) irrespective of the h -refinement utilized.

Figs. 22–24 show the fields of the transverse shear stresses at the reference surface obtained from integration, for all three models. The FEM results are discontinuous, with a constant value in each element, as expected, since the basis are of second degree and the integration involves derivatives of the in-plane stresses. The C^0 -GFEM shows a discontinuous but very smooth response. The C^k -GFEM results for shear stresses obtained from the integration, in Fig. 24(a), shows peaks at the surface. These peaks are probably due to the behavior of the second derivatives of the basis functions. Fig. 24(b) shows the results for shear stresses obtained from the process of correction with the transverse shear force. This correction smoothes the results, in the same way as seen in Fig. 21 along the boundary of the laminated plate.

5. Conclusions

A generalized finite element method based on a partition of unity (PoU) with smooth approximation is developed in this paper to model laminated plates under the Mindlin kinematic

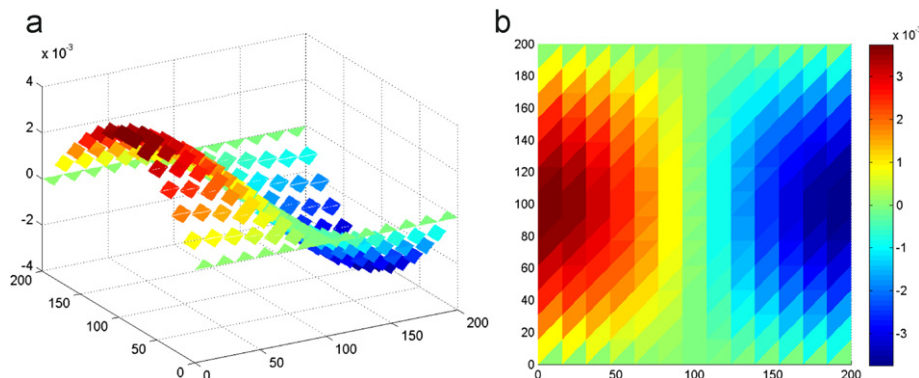


Fig. 22. Transverse shear stress τ_{xz}^i by integration, from FEM, at coordinate $z=0$.

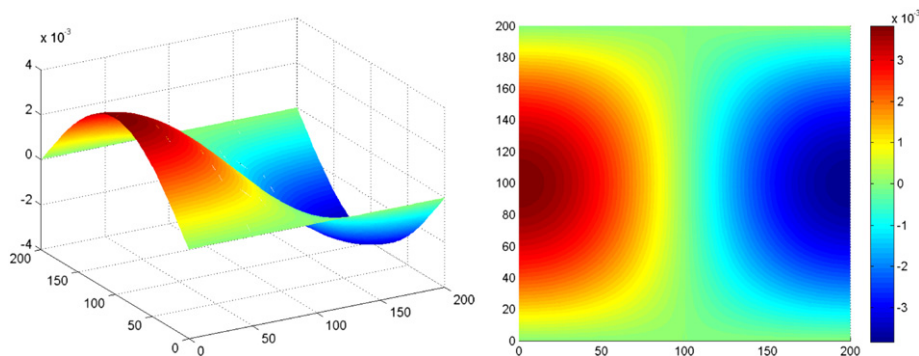


Fig. 23. Transverse shear stress τ_{xz}^i from C^0 -GFEM by integration, at coordinate $z=0$.

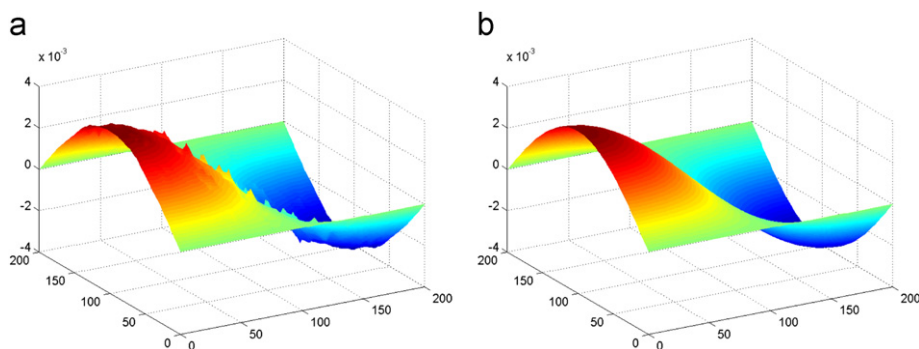


Fig. 24. Transverse shear stress at coordinate $z=0$, from C^k -GFEM with C^∞ partition of unity. τ_{xz}^i is obtained by (a) integration and (b) by using shear force correction.

hypothesis, generating a set of enriched shape functions capable to result in arbitrarily continuous in-plane stresses everywhere in the domain. The formulation possess the following characteristics:

(i) The shape functions are obtained from enrichment of PoU ones. The enrichment functions are of the polynomial type and defined in global coordinates. The PoU is defined in global coordinates but with compact support, such that the enrichment degree can be specified independently in each region of the mesh, making the procedure appropriate for adaptive schemes.

(ii) The proposed formulation proved to be able to approximate the solution of anisotropic laminated Mindlin plate problems with the prescribed degree of continuity in the displacement and stress fields. In particular, in-plane and transverse shear stresses are obtained with arbitrary smoothness degree and with excellent agreement with analytical solutions. Even though the paper concentrates all its numerical results on the bending phenomenon the formulation is complete, including all the coupling effects between bending and membrane, as is required in the analysis of anisotropic composites. Therefore, the formulation is equally able to deal with purely membrane problems. The reason for concentrating on bending is that the ever present difficulties associated with accurate transverse shear stress computations are traditionally addressed in bending studies.

(iii) Compared with the standard FEM, the continuous GFEM has a more elaborate formulation, but shows about the same level of complexity as the C^0 -GFEM, except in its elaborated form to compute the PoU. The demand for more integration points is associated with increased CPU time instead of formulation complexity. In fact, all the particular details of the formulation can be encapsulated in a well delimited set of program routines, whose final result is the set of values for the basis functions and their derivatives at an integration point, which, as in the FEM, are used in the standard way in the computation of the deformation matrices.

(iv) The approximation functions generated by the present procedure have complex shapes with large plateaus and sharp hills, such that their derivatives are still more irregular in shape. As a result, the amount of numerical effort required to perform an adequate evaluation of the coefficients of the stiffness matrix is of concern. The results show that the edge functions of the polynomial type require less integration points for the lower degrees. However, these polynomial degrees also define the level of continuity of the shape functions generated. Since the weak form of the Mindlin plate problem requires $C^0(\Omega)$ displacement functions, the polynomial with a degree of one is the simplest polynomial edge function possible, which generates a discontinuous in-plane stress response. In this study, surprisingly, it was found that similar integration difficulties are associated with the Mindlin model, similar to the Kirchhoff counterpart as reported in [39], but to different extents.

(v) $C^k(\Omega)$ continuous in-plane stress approximations are obtained using $k+1$ degree polynomial edge functions. If one is interested in $C^k(\Omega)$ continuous transverse shear stress approximations, it is necessary to use $k+2$ degree polynomial edge functions. In parallel, instead of the polynomial edge functions, the exponential ones can be used, which generates $C^\infty(\Omega)$ fields in convex clouds.

(vi) In clouds with pairs of non-convex edges, the continuity of the shape functions generated in the method are limited to $C^k(\Omega)$, with k arbitrary and $k \geq 0$. This lower continuity applies only at the corner between the two non-convex edges. Everywhere else on the edges, the continuity is defined by the selected type of edge functions. Clearly, the value of k does not affect the computational cost.

(vii) The heuristic procedure proposed to post-process the transverse shear stress was shown to be able, in the numerical experiments, to smoothen the distributions and to improve the accuracy of the transverse shear stresses.

(vii) The required number of integration points for the approximation functions generated from the exponential edge functions are similar to those of polynomials of degree 2 or 3. The integration effort varies with the enrichment degree, the plate thickness and mesh distortion.

(viii) The results show sensitivity with the plate thickness, although no special care was taken to prevent shear locking. Consistent results are obtained with aspect ratios length/thickness of between 4 and 1000, for enrichment degrees 2, 3 and 4.

(ix) The results of both formulations, standard and continuous GFEM, show excellent ability to withstand high mesh distortion. Consistent results are obtained when meshes built of elements with aspect ratios of 1:1 to 9800:1 are used. For a given degree of the most complete polynomial the basis can represent, the continuous GFEM shows better results than those for the standard GFEM/ XFEM, although it requires more degrees of freedom operations. However, the preset PoU is much less computationally expensive than most meshless methods like *hp*-clouds and element-free Galerkin methods, which are usual alternatives for C^k or C^∞ approximation functions.

(x) In general, the results show that the continuous GFEM behaves similarly to the standard GFEM with regard to complexity of formulation, accuracy, resilience to mesh distortion and condition number. The former shows some improved accuracy for similar basis and mesh distortion. Therefore, the formulation is appropriate to discretize boundary value problems, where the continuous basis is used to approximate the variables which require higher-order continuity and the standard GFEM/ XFEM to approximate the C^0 variables.

Acknowledgements

We gratefully acknowledge the support provided by the Brazilian government agency Conselho Nacional de Desenvolvimento Científico e Tecnológico (CNPq) for the Research Projects N.309.640/2006-7, N.303.315/2009-1 and N.303.575/2010-7.

References

- [1] J. Dolbow, N. Moës, T. Belytschko, Modeling fracture in Mindlin–Reissner plates with the extended finite element method, *Int. J. Solids Struct.* 37 (2000) 7161–7183.
- [2] K.J. Bathe, *Finite Element Procedures*, Prentice-Hall/MIT, Englewood Cliffs, 1996.
- [3] B.F. Veubeke, G. Sander, An equilibrium model for plate bending, *Int. J. Solids Struct.* 4 (1968) 447–468.
- [4] S.W. Lee, C. Wong, Mixed formulation finite elements for Mindlin plate bending, *Int. J. Numer. Methods Eng.* 18 (1982) 1297–1311.
- [5] T.J.R. Hughes, T. Tezduyar, Finite Elements based upon Mindlin plate theory with particular reference to the four-node isoparametric element, *J. Appl. Mech. Trans. ASME* 48 (1981) 587–596.
- [6] K. Bletzinger, M. Bischoff, E. Ramm, A unified approach for shear-locking-free triangular and rectangular shell finite elements, *Comput. Struct.* 75 (2000) 321–334.
- [7] G.R. Liu, K.Y. Dai, T.T. Nguyen, A smoothed finite element for mechanics problems, *Comput. Mech.* 39 (2007) 859–877.
- [8] H. Nguyen-Xuan, T. Rabczuk, S. Bordas, J.F. Debonnie, A smoothed finite element method for plate analysis, *Comput. Methods Appl. Mech. Eng.* 197 (2008) 1184–1203.
- [9] O.A. Garcia, E.A. Fancello, C.S. de Barcellos, C.A. Duarte, *hp*-Clouds in Mindlin's thick plate model, *Int. J. Numer. Methods Eng.* 47 (2000) 1381–1400.
- [10] P. Krysl, T. Belytschko, Analysis of thin plates by the element-free-Galerkin method, *Comput. Mech.* 16 (1995) 1–10.
- [11] Q. Li, J. Soric, T. Jarak, S.N. Atluri, A locking-free meshless local Petrov–Galerkin formulation for thin and thick plates, *J. Comput. Phys.* 208 (2005) 116–133.
- [12] J. Soric, Q. Li, T. Jarak, S.N. Atluri, The meshless local Petrov–Galerkin (MLPG) formulation for analysis of thick plates, *Comput. Model. Eng. Sci.* 6 (2004) 349–357.
- [13] D. Wang, S.B. Domg, J.S. Chen, Extended meshfree analysis of transverse and inplane loading of a laminated anisotropic plate of general planform geometry, *Int. J. Solids Struct.* 43 (2006) 144–171.
- [14] L.M.J.S. Dinis, R.M. Natal Jorge, J. Belinha, Analysis of plates and laminates using natural radial point interpolation method, *Eng. Anal. Boundary Elem.* 32 (2008) 267–279.
- [15] R.A. Gingold, J.J. Monaghan, Kernel estimates as a basis for general particle methods in hydrodynamics, *J. Comput. Phys.* 46 (1982) 429–453.
- [16] B. Nayroles, G. Touzot, P. Villon, Generalizing the finite element method: diffuse approximation and diffuse elements, *Comput. Mech.* 10 (1992) 307–318.
- [17] K. Amarantuga, J.R. Williams, S. Quan, J. Weis, Wavelet-Galerkin solutions for one-dimensional partial differential equations, *Int. J. Numer. Methods Eng.* 37 (1994) 2703–2716.
- [18] T. Belytschko, Y.Y. Lu, J. Gu, Crack propagation by element free Galerkin methods, in: *Advanced Computational Methods for Material Modeling*, AMD-vol. 180/PVP-vol. 268, ASME, 1993, pp. 191–205.
- [19] W.K. Liu, S. Jun, Y. Zhang, Reproducing kernel particle methods, *Int. J. Numer. Methods Fluids* 20 (1995) 1081–1106.
- [20] S.N. Atluri, T. Zhu, New meshless local Petrov–Galerkin (MLPG) approach in computational mechanics, *Comput. Mech.* 22 (1998) 117–127.
- [21] N. Sukumar, B. Moran, T. Belytschko, The natural element method, *Int. J. Numer. Methods Eng.* 43 (1998) 839–887.
- [22] I. Babuška, J.M. Melenk, The partition of unity method, Technical Note BN-1185, Institute for Physical Science and Technology, University of Maryland, 1995.
- [23] C.A. Duarte, J.T. Oden, *hp* Clouds—a meshless method to solve boundary value problems, TICAM Report 95-05, University of Texas, 1995.
- [24] C.A. Duarte, J.T. Oden, *hp* Clouds—an *hp* meshless method, *Numer. Methods Partial Differential Equations* 12 (1996) 673–705.
- [25] L.C. Nicolazzi, C.A. Duarte, E.A. Fancello, C.S. de Barcellos, *hp*-Clouds—a meshless method in boundary elements. Part II: implementation, *Int. J. Boundary Elem. Method Commun.* 8 (1997) 83–85.
- [26] J.T. Oden, C.A. Duarte, O.C. Zienkiewicz, A new cloud-based *hp* finite element method, *Comput. Methods Appl. Mech. Eng.* 153 (1998) 117–126.
- [27] J.M. Melenk, On generalized finite element methods, Ph.D. Dissertation, University of Maryland, 1995.
- [28] I. Babuška, J.M. Melenk, The partition of unity finite element method: basic theory and applications, *Comput. Methods Appl. Mech. Eng.* 139 (1996) 289–314.
- [29] T. Belytschko, T. Black, Elastic crack growth in finite elements with minimal remeshing, *Int. J. Numer. Methods Eng.* 45 (1999) 601–620.
- [30] N. Moës, J. Dolbow, T. Belytschko, Elastic crack growth in finite elements without remeshing, *Int. J. Numer. Methods Eng.* 46 (1999) 131–150.
- [31] T. Belytschko, R. Gracie, G. Ventura, A review for extended/generalized finite element methods for material modeling, *Modelling Simul. Mater. Sci. Eng.* 17 (2009) 23–25. doi:10.1088/0965-0393/17/4/043001.
- [32] T. Strouboulis, K. Copps, I. Babuska, The generalized finite element method, *Comput. Methods Appl. Mech. Eng.* 190 (2001) 4081–4193.
- [33] T. Strouboulis, L. Zhang, I. Babuska, Generalized finite element method using mesh-based handbooks: applications to problems in domains with many voids, *Comput. Methods Appl. Mech. Eng.* 192 (2003) 3109–3161.
- [34] C.A. Duarte, I. Babuska, Mesh-independent *p*-orthotropic enrichment using the generalized finite element method, *Int. J. Numer. Methods Eng.* 55 (2002) 1477–1492.
- [35] F.B. Barros, S.P.B. Proença, C.S. de Barcellos, On error estimator and *p*-adaptivity in the generalized finite element method, *Int. J. Numer. Methods Eng.* 60 (2004) 2373–2398.
- [36] F.B. Barros, C.S. de Barcellos, C.A. Duarte, *p*-Adaptive C^k generalized finite element method for arbitrary polygonal clouds, *Comput. Mech.* 41 (2007) 175–187.
- [37] A. Simone, C.A. Duarte, E. Van der Giessen, A generalized finite element method for polycrystals with discontinuous grain boundaries, *Int. J. Numer. Methods Eng.* 67 (2006) 1122–1145.
- [38] O.A. Garcia, E.A. Fancello, P.T.R. Mendonça, Developments in the application of the generalized finite element method to thick shell problems, *Comput. Mech.* 44 (2009) 669–682.
- [39] C.S. de Barcellos, P.T.R. Mendonça, C.A. Duarte, A C^k continuous generalized finite element formulation applied to laminated Kirchhoff plate model, *Comput. Mech.* 44 (2009) 377–393.
- [40] D.A.F. Torres, P.T.R. Mendonça, C.S. de Barcellos, Evaluation and verification of an HSDT-layerwise generalized finite element formulation for adaptive piezoelectric laminated plates, *Comput. Methods Appl. Mech. Eng.* 200 (2011) 675–691.
- [41] C.A. Duarte, O.N. Hamzeh, T.J. Liszka, W.W. Tworzydło, A generalized finite element method for the simulation of three-dimensional dynamic crack propagation, *Comput. Methods Appl. Mech. Eng.* 190 (2001) 2227–2262.
- [42] H.C. Edwards, C^∞ finite element basis functions. Technical Report, TICAM Report 96-45, The University of Texas at Austin, 1996.
- [43] H.C. Edwards, A Parallel infrastructure for scalable adaptive finite element methods and its application *hp* least squares C^∞ collocation, Ph.D. Dissertation, The University of Texas at Austin, 1997.
- [44] C.A. Duarte, D.J. Kim, D.M. Quaresma, Arbitrarily smooth generalized element approximations, *Comput. Methods Appl. Mech. Eng.* 196 (2006) 33–56.
- [45] V.L. Rvachev, T.I. Sheiko, R-functions in boundary value problems in mechanics, *Appl. Mech. Rev.* 48 (1995) 151–188.
- [46] V. Shapiro, Theory of R-functions and applications: a primer, Technical Report TR91-1219, Computer Science Department, Cornell University, Ithaca, NY, 1991.

- [47] R. Actis, B.A. Szabo, C. Schwab, Hierarchic models for laminated plates and shells, *Comput. Methods Appl. Mech. Eng.* 172 (1999) 79–107.
- [48] I. Babuska, M. Suri, The optimal convergence rate of the p version of the finite element method, *SIAM J. Numer. Anal.* 24 (1987) 750–776.
- [49] I. Babuska, U. Banerjee, J.E. Osborn, Q. Zhang, Effect of numerical integration on meshless methods, *Comput. Methods Appl. Mech. Eng.* 198 (2009) 2886–2897.
- [50] D. Shepard, A two-dimensional function for irregularly spaced data, in: *ACM National Conference*, 1968, pp. 517–524.
- [51] T. Belytschko, W.K. Liu, M. Singer, On adaptivity and error criteria for mesh free methods, in: P. Ladèveze, J.T. Oden (Eds.), *Advances in Adaptive Computational Methods in Mechanics*, 1998, pp. 217–228.
- [52] C.A. Duarte, I. Babuška, J.T. Oden, Generalized finite element method for three-dimensional structural mechanics problems, *Comput. Struct.* 77 (2000) 215–232.
- [53] R.D. Mindlin, Influence of rotary inertia and shear on flexural motion of isotropic elastic plates, *J. Appl. Mech.* 18 (1951) 336–3343.
- [54] J.N. Reddy, *Mechanics of Laminated Composite Plates and Shells*, second ed., CRC Press, Boca Raton, 1997.
- [55] A.L. Dobyns, The analysis of simply-supported orthotropic plates subjected to static and dynamic loads, *Am. Inst. Aeronaut. Astronaut. J.* 19 (1981) 642–650.
- [56] J.N. Reddy, A simple higher-order theory for laminated composite plates, *J. Appl. Mech.* 51 (1984) 745–752.
- [57] N.J. Pagano, Exact solutions for rectangular bidirectional composites and sandwich plates, *J. Comput. Mater.* 4 (1970) 20–35.
- [58] D.A. Dunavant, High degree efficient symmetrical Gaussian quadrature rules for the triangle, *Int. J. Numer. Methods Eng.* 21 (1985) 1129–1148.
- [59] S. Wandzura, H. Xiao, Symmetric quadrature rules on a triangle, *Comput. Math. Appl.* 45 (2003) 1829–1840.
- [60] T. Strouboulis, I. Babuška, K. Copps, The design and analysis of the generalized finite element method, *Comput. Methods Appl. Mech. Eng.* 181 (2000) 43–69.